scientific reports

OPEN

Characterization and machine learning based optimization of banana and paddy straw fiber reinforced epoxy hybrid composites

Saravanakumar Sengottaiyan[1], M. Muhemin Sheriff[2], V. S. Shaisundaram[3], Yuvaraj Dinakarkumar[4], S. Ramalakshmi[5] & S. Rajkumar[6,7]✉

This paper investigates a novel hybrid epoxy composite reinforced with cellulose-rich banana and paddy straw fibers, focusing on its fabrication and machining characteristics. While natural fibers have been widely studied, hybrid epoxy composites reinforced with banana and paddy straw fibers remain underexplored. The composites were evaluated for mechanical properties (tensile, flexural, and impact), thermal stability, and water absorption, revealing that the formulation with 30% banana fiber and 10% paddy straw fiber (BP2) provided the best overall balance of tensile, flexural, impact, thermal, and moisture-resistance properties among the compositions studied. Machinability was assessed using Abrasive Water Jet Machining (AWJM), where process parameters, abrasive flow rate (AFR), traverse speed (TS), and standoff distance (SoD), were optimized using Response Surface Methodology (RSM) and Artificial Neural Networks (ANN). The optimal conditions (AFR = 400 g/min, TS = 250 mm/min, SoD = 3 mm) resulted in reduced surface roughness (SR = 3.60 µm) and kerf angle (Kf = 1.56°). SEM, FTIR, and XRD analyses confirmed improved fiber-matrix bonding in BP2, correlating with enhanced machining performance. AWJM provided good machining performance for the developed hybrid composite, achieving low surface roughness and a controlled kerf angle under optimized conditions. This study demonstrates the potential of hybrid banana-paddy straw composites in sustainable engineering, particularly when optimized machining techniques are applied.

Keywords Hybrid biocomposites, Mechanical properties, Thermal degradation, Abrasive water jet machining, Artificial neural network

Fiber-reinforced polymer composites with biodegradable components have attracted attention for their environmental friendliness, affordability, and strong mechanical properties[1,2]. Recent literature has emphasized sustainable epoxy hybrid composites for lightweight engineering applications, multiscale modeling strategies for natural fiber-reinforced systems, and the influence of weathering on the long-term behavior of hybrid epoxy composites[3–5]. These studies broaden the scientific context of the present work and further support the relevance of developing banana–paddy straw fiber reinforced epoxy composites for sustainable structural applications[6,7]. Although naturally reinforced composites are weaker than carbon-fiber systems, they offer significant advantages in weight, cost, and environmental impact when these factors outweigh performance demands[8–10]. Hybrid composites leverage multiple natural fibers to enhance mechanical properties; combining banana and

[1]Faculty of Engineering and Technology, Villa College, Male, Maldives. [2]Artificial Intelligence and Machine learning (AI&ML) Department, Easwari Engineering College, Ramapuram, Chennai, Tamil Nadu, India. [3]Department of Mechanical Engineering, Vels Institute of Science, Technology and Advanced Studies (VISTAS), Chennai, Tamil Nadu, India. [4]Department of Biotechnology, School of Life Sciences, Vels Institute of Science, Technology and Advanced Studies (VISTAS), Chennai, Tamil Nadu, India. [5]Department of Bioengineering, School of Engineering, Vels Institute of Science, Technology and Advanced Studies (VISTAS), Chennai, Tamil Nadu, India. [6]Department of Mechanical Engineering, Faculty of Manufacturing, Institute of Technology - Hawassa University, Hawassa, Ethiopia. [7] Centre for Research and Innovation, Academy of Maritime Education and Training (AMET) Deemed to be University, Kanathur, Chennai 603112, Tamil Nadu, India. ✉email: rajkumar@hu.edu.et

paddy straw fibers, abundant agricultural waste, provides economic and sustainability benefits through waste utilization[11–13]. These composites serve automotive, aeronautical, and construction applications, but machining hybrid materials poses challenges for conventional methods due to heterogeneous fiber–matrix behavior, leading to delamination, fiber pull-out, and poor surface control[14,15]. Abrasive Water Jet Machining (AWJM), a cool, non-contact process, reduces heat damage and tool wear, making it suitable for precision composite machining[16,17]. Machine learning and Response Surface Methodology (RSM) enable rapid optimization of AWJM parameters by reliably predicting machining responses across large parameter spaces without extensive experimentation[18–20].

In this study, hybrid composites are produced using banana and paddy straw fibres in an epoxy matrix, combining the relatively high tensile strength of banana fibres (110 to 150 MPa)[21,22] with the low weight and environmentally favourable character of paddy straw fibres (40 MPa to 100 MPa)[23,24]. The work evaluates the mechanical performance of these hybrids, develops hyperparameter-tuned machine learning models, and uses both ML and RSM to optimise AWJM parameters to improve machining accuracy and efficiency[25]. This approach supports sustainable engineering by converting agricultural waste into value-added composite materials. Cellulose-rich polysaccharides in banana and paddy straw have distinct crystallinity and branching, which can influence thermal stability, moisture interactions, and reinforcement efficiency in polymer matrices, and these factors may affect both composite performance and machining response[26].

Earlier AWJM studies on natural-fiber composites consistently identify stand-off distance (SoD) and traverse speed (TS) as dominant factors controlling surface roughness (SR) and kerf geometry, with pressure and abrasive characteristics playing secondary roles[27]. For banana–polyester laminates, SoD accounted for 60.6% of SR and 74.8% of kerf angle, highlighting the need for strict SoD control to reduce taper. Subsequent work on banana and other natural-fiber systems confirmed that abrasive size, TS, and pressure jointly influence kerf width, taper, and material removal rate, emphasizing abrasive–jet energy coupling and material architecture effects[28–30] However, these studies generally examine single-fiber or filled laminates and rely mainly on Taguchi or RSM approaches, with limited use of advanced predictive models[31,32].

Against this background, the present work investigates a hybrid banana–paddy straw epoxy composite and uses both ANN and RSM to capture nonlinear interactions among AFR, TS, and SoD during AWJM. Under optimised conditions of AFR = 400 g/min, TS = 250 mm/min, and SoD = 3 mm, the system achieves SR = 3.60 μm and Kf = 1.56°, aligning with banana-based benchmarks while avoiding the thermal defects often associated with laser-based routes. The observed sensitivities, especially the prominence of SoD and TS, and the ability of Artificial Neural Network (ANN) models to capture nonlinear interactions, are consistent with prior work, while the specific agricultural waste hybrid composition is distinct and has not been previously examined.

Although banana-fiber composites, paddy-straw composites, hybrid natural-fiber epoxy systems, and AWJM optimization studies have all been reported individually in the literature, their combined study in the present banana–paddy straw epoxy system remains limited. Therefore, the contribution of this work is not claimed as a completely new class of composite or a new optimization methodology. Rather, this study provides a focused material-specific investigation that links composition selection, microstructural features, mechanical and thermal behavior, moisture response, and AWJM performance of banana–paddy straw hybrid epoxy laminates. In addition, AWJM studies on natural fibre composites commonly rely on Taguchi or RSM, with limited use of advanced predictive modelling. To address these gaps, this work develops a new banana and paddy straw hybrid epoxy composite, evaluates its tensile, flexural, and impact properties along with thermal behaviour and water absorption, and presents the first AWJM investigation for this material. The study also differs from earlier work[33,34], which focused on banana and roselle fibre epoxy composites containing alumina and boiled eggshell fillers. While the use of AWJM, RSM, and ANN is well established in the literature, the present study's contribution lies in applying these tools to the banana–paddy straw hybrid epoxy composite and relating the optimal machining response of BP2 to its improved microstructural integrity and fiber–matrix bonding.

Materials and methods

Fabrication of materials

Banana pseudostems and paddy straw were collected, washed, dried, and mechanically processed into fibers. For composite fabrication, the banana fibers were arranged as matted fiber layers, whereas the paddy straw fibers were used in randomly oriented form (Fig. 1 and 2). In the present study, no alkali or silane surface treatment was applied to either the banana or paddy straw fibers. The fibers were used after washing, drying, and mechanical preparation in order to evaluate the baseline performance of the hybrid composite without additional chemical modification variables. This approach was also chosen to maintain a simple, low-cost, and sustainable fabrication route based on minimally processed agricultural fibers.

Epoxy resin (LY556) and hardener (HY951) were used as the matrix system due to their compatibility with natural fiber-reinforced composites. The epoxy system was procured from M/s Fiber Region, Chennai. The compositions of the fabricated laminates are listed in Table 1 and are expressed as nominal weight percentages (wt%) of epoxy, banana fiber, and paddy straw fiber, based on the initial weighed quantities used during fabrication. No separate post-consolidation fraction verification was performed in this study.

The present study was designed around the hypothesis that the banana-to-paddy-straw fiber ratio would significantly influence the overall performance of the hybrid epoxy composite. Specifically, increasing banana fiber content was expected to improve load transfer and mechanical strength, whereas excessive paddy straw content was expected to increase hydrophilicity and reduce interfacial efficiency. Accordingly, three representative formulations were selected. BP1 represented a 70/30 matrix/fiber composition, while BP2 and BP3 represented 60/40 matrix/fiber compositions with different banana-to-paddy-straw ratios. These formulations were selected based on the authors' earlier studies on banana-fiber epoxy and hybrid natural-fiber composites, in which 70/30

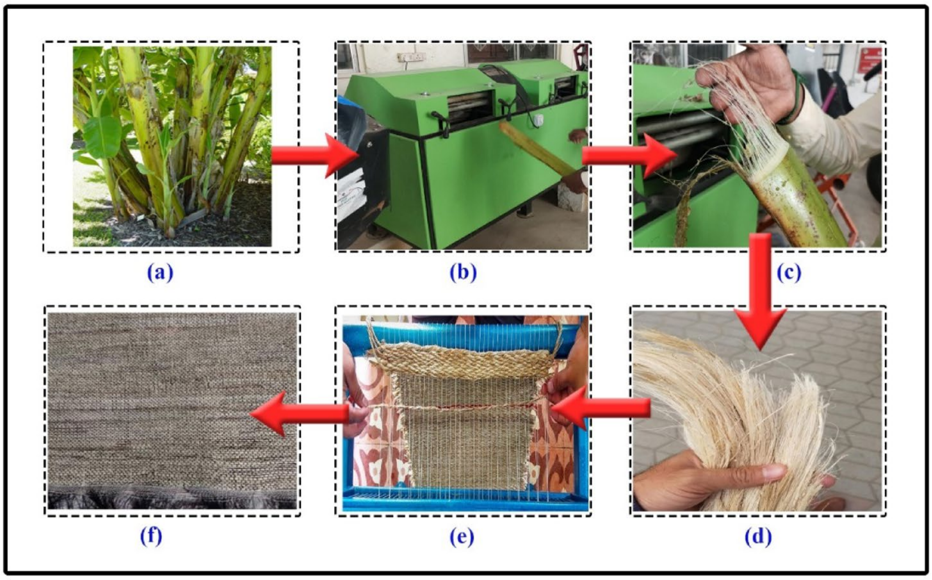

Fig. 1. Mechanical extraction and preparation of banana fiber for composite fabrication.

Fig. 2. Collection and preparation of paddy straw fiber used in a randomly oriented form for composite fabrication.

S.No	Composition	Abbreviation
1	Epoxy (70%) + Banana Fiber (20%) + Paddy straw (10%)	BP1
2	Epoxy (60%) + Banana Fiber (30%) + + Paddy straw (10%)	BP2
3	Epoxy (60%) + Banana Fiber (25%) + + Paddy straw (15%)	BP3

Table 1. Nominal composition of fabricated laminates in weight% (wt%).

and related higher-fiber-loading compositions showed favorable mechanical performance. Thus, the present work employed a focused composition window rather than an exhaustive screening of all possible formulations.

For fabrication, a composite charge consisting of banana fiber mats, randomly oriented paddy straw fibers, epoxy resin, and hardener was placed into the preheated mould. The moulding temperature was maintained at 150 °C, and a pressure of 20 bar was applied to ensure proper consolidation and curing of the resin system. After compression molding, the laminate plates were removed from the mold, cooled, and post-cured under ambient conditions before being cut into test specimens for further characterization. This method enabled the effective production of banana and paddy straw fiber-reinforced epoxy composites. Three laminates (BP1-BP3) (supplementary Fig. 1) were selected as representative formulations based on the authors' earlier studies on banana-fiber epoxy and hybrid natural-fiber composites, where 70/30 matrix/fiber loading and related higher-fiber hybrid compositions showed favorable mechanical performance[35].

Materials characterization

The banana-paddy straw hybrid composites were tested for tensile, flexural, and impact properties, and supplemented by thermal, physical, and structural analyses. Tensile testing was performed on a UNITEK universal testing machine in accordance with ASTM D638-10, using specimens of $165 \times 25 \times 3$ mm³ at a crosshead speed of 5 mm/min. ASTM D638 was used here for comparative tensile evaluation of the molded reinforced-epoxy coupons. Specimens were cut from the post-cured plates to the required dimensions, and only coupons free from visible edge defects were used for testing. Flexural strength testing was done using an Instron 3382 machine in compliance with ASTM D790-07, and impact testing was performed according to ASTM D256 using an Izod pendulum impact tester (XJJU-5.5) on unnotched specimens of $65 \times 12.7 \times 3$ mm³, with a pendulum capacity of 0.1–14 J[36]. For each composition, three specimens were tested for tensile, flexural, and impact characterization, and the reported values represent the mean of three measurements. To determine the environmental durability, water absorption tests were conducted according to ASTM D570[37], in the specimens were submerged in distilled water, and the percentage weight gain was observed with time.

A Thermogravimetric Analysis (TGA) was performed to examine thermal degradation behavior and provide additional information on the decomposition stages and thermal stability. Water absorption was evaluated as a comparative gravimetric immersion test to assess the moisture uptake behavior of the BP1-BP3 laminates. The present study did not include diffusion coefficient calculations or Fickian/non-Fickian kinetic modeling; therefore, the water-absorption results are discussed only in terms of relative uptake trends and equilibrium behavior. To determine functional groups and chemical interactions, Microstructural and bonding mechanisms were explored using Fourier Transform Infrared Spectroscopy (FTIR) and X-ray Diffraction (XRD) to assess crystallinity and phase compositions of fibers and composites. The combination of these tests determines the mechanical, thermal, and moisture resistance, as well as the interfacial properties of the composites. It provides a complete assessment of their suitability for advanced applications.

Abrasive waterjet machining

Abrasive Water Jet Machining (AWJM) experiments were conducted on the BP2 laminate to investigate the effects of selected machining parameters on surface roughness (SR) and kerf angle (Kf). The three variable process parameters were abrasive flow rate (AFR: 200, 300, and 400 g/min), traverse speed (TS: 150, 200, and 250 mm/min), and standoff distance (SoD: 2, 3, and 4 mm). During all machining trials, the abrasive type (garnet), nozzle diameter (0.76 mm), and waterjet pressure were kept constant to ensure uniform machining conditions and to isolate the effects of AFR, TS, and SoD. Thus, the experimental design specifically evaluated the influence of these three input variables while maintaining the remaining AWJM conditions unchanged. Due to its hardness and cutting ability, garnet is an abrasive material. Certain attributes are required to determine the effectiveness and efficiency of the AWJM process. The variables selected to achieve the highest surface polish and dimensional accuracy, and to minimize flaws in the machined parts, are waterjet pressure, AFR, TS, SoD, and abrasive type (Garnet). These parameters were chosen based on prior knowledge of AWJM principles and empirical evidence from experimental research.

Surface roughness (SR)

The Mitutoyo Surftest SJ-401 instrument, with a 5 mm sampling length, is used to quantify surface roughness (SR) of cut surfaces. The equipment classifies surface roughness into three zones: smooth, transitional, and rough, with a measurement range of 350 μm and a speed of 0.25 mm/s[38]. This study particularly assesses SR, the arithmetic average roughness, in transition along the circular cutting direction.

Kerf angle (Kf)

Another output response that is used to evaluate the specimen's dimensional correctness is the kerf angle[34,38], which is computed using the following Eq. (1):

$$\tan\theta^\circ = \frac{TW - BW}{2t} \tag{1}$$

Where:

- TW represents the Top Kerf Width,
- BW represents the Bottom Kerf Width, and.
- t represents the Thickness of the specimen.

Prediction and optimization of AWJM performance
ANN modeling and RSM were used to predict and optimize the performance of the banana and paddy straw hybrid epoxy composite. Surface Roughness (SR) and Kerf Angle (Kf) were examined in relation to the three levels of variation in key AWJM parameters, including AFR, TS, and SoD. To determine the optimal network architecture, an ANN model was developed using Python, TensorFlow, and Keras[39]. A grid search model was used to optimize the hyperparameters. High predictive accuracy was achieved after training and testing the ANN model on experimental and unseen data. To determine the optimal factor levels, RSM fitted a quadratic equation and generated response surface plots to identify the best levels. Although the ANN model is more flexible in modeling nonlinear interactions, as it can be adapted to the data requirements and trained directly on the data, its prediction accuracy is higher than RSM, with higher R-squared (R^2) values and lower MAE. Although the ANN dataset comprised 135 data points, the network architecture was optimized via a grid search to identify the most suitable model structure. In addition, batch normalization was incorporated during training to improve model stability and reduce the risk of overfitting. Nevertheless, these limitations do not render RSM an unprofitable method for revealing parameter interactions and for providing clear statistical information to enhance the predictive capabilities of ANN.

Results and discussion
FTIR and XRD analysis
Figure 3a shows that the FTIR spectra of banana fiber and paddy straw contain broad O–H stretching bands at approximately 3340 cm^{-1} and C–H stretching vibrations near 2915 cm^{-1}, which are characteristic of cellulose and hemicellulose. The band around 1730 cm^{-1} is assigned to the C = O stretching of hemicellulose-related acetyl/ester groups, while lignin contributes bands near 1240–1260 cm^{-1}. For the LY556/HY951 epoxy system, the matrix is more appropriately identified through the characteristic epoxy/ether/aromatic features of the resin system rather than by a strong carbonyl band. Therefore, the previous assignment of a strong epoxy C = O absorption at ~ 1725 cm^{-1} has been removed. In the hybrid composites (BP1–BP3), particularly BP2, the reduction and slight shifting of the fiber-related O–H and carbonyl bands indicate improved interfacial interaction between

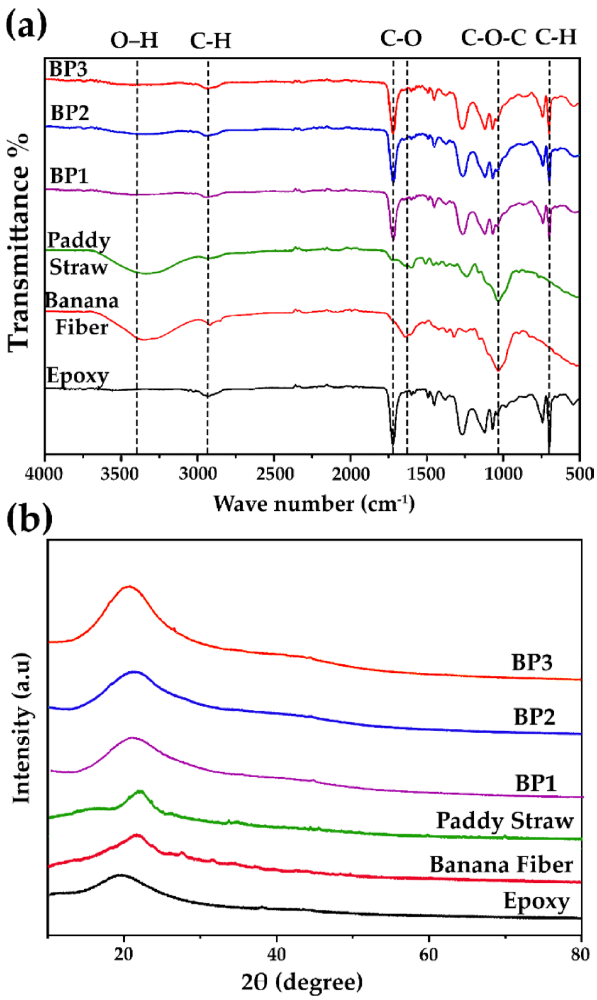

Fig. 3. (**a**) FTIR spectra and (**b**) XRD patterns of epoxy, banana fiber, paddy straw, and hybrid composites (BP1–BP3).

the banana/paddy straw fibers and the epoxy matrix, consistent with hydrogen bonding and partial shielding of fiber surface groups by the matrix. Gokul Kannan and Thangararaju[40] observed similar spectral changes in banana-coconut shell composites, which suggest improved interfacial adhesion due to hydrogen bonding and chemical compatibility.

Figure 3b's XRD patterns of the natural fibers show a clear cellulose I peak at 22° 2θ, indicating a semi-crystalline structure, while epoxy appears as a broad amorphous halo. In the BP composites, the peaks at 22° 2θ are still visible but with reduced intensity, confirming the semi-crystalline nature of these hybrids. Therefore, FTIR was used to indicate chemical compatibility, while XRD suggested slightly greater structural ordering in BP2. Together with the SEM observations, these results provide qualitative support for the improved mechanical and machining behavior of BP2. However, because no direct quantitative correlation analysis was performed, the relationships among crystallinity, interfacial bonding, and machinability should be interpreted cautiously. Similar results were reported by Indran et al.[21] who linked higher cellulose crystallinity to increased thermal resistance in banana peel cellulose, and by Arumika Prabu et al.[28], who associated crystallinity with improved machinability in banana fiber composites. Therefore, FTIR was used to confirm chemical compatibility, while XRD demonstrated that the optimized hybridization process (BP2) increased structural ordering, directly supporting the observed improvements in strength and AWJM machinability.

Mechanical test analysis

Mechanical property tests, including tensile, flexural, and impact strengths, were conducted to assess the mechanical properties of the three laminate designs (BP1, BP2, and BP3). The mechanical property values shown in Fig. 4 are reported as mean values of three specimens, and the error bars represent the standard deviation. The results show clear trends in mechanical performance that are linked to variations in fiber composition and content. BP2 showed the highest average tensile strength among the tested compositions (33.54 MPa), followed closely by BP3 (31.87 MPa) and BP1 (25.34 MPa). Since no statistical significance analysis was performed in the present study, the difference between BP2 and BP3 should be interpreted cautiously. Nevertheless, the observed trend is qualitatively consistent with the SEM results, which indicate better fiber embedding, fewer voids, and improved interfacial bonding in BP2. The greater percentage of banana fibers in BP2 likely contributes to its effectiveness in resisting tensile stresses, as the material is very strong in tension. Conversely, BP1 had the lowest tensile strength due to its lower banana fiber content (20%), resulting in weaker fiber-matrix interactions and reduced reinforcement. In terms of flexural strength, BP2 again outperformed the others with 51.65 MPa, compared to BP3's 47.43 MPa and BP1's 36.87 MPa. BP2's higher flexural strength is attributed to its higher banana fiber content, which provides excellent stiffness and resistance to bending. BP3, with slightly less banana fiber (25%) and more paddy straw (15%), showed slightly lower flexural strength than BP2.

The positive impact of banana and paddy straw fibers on the composite's strength was evident, demonstrating a significant improvement over BP1. The lower flexural strength of BP1 suggests that its reduced fiber content limits its capacity to resist bending deformation. Regarding impact strength, BP2 recorded the highest at 25.76

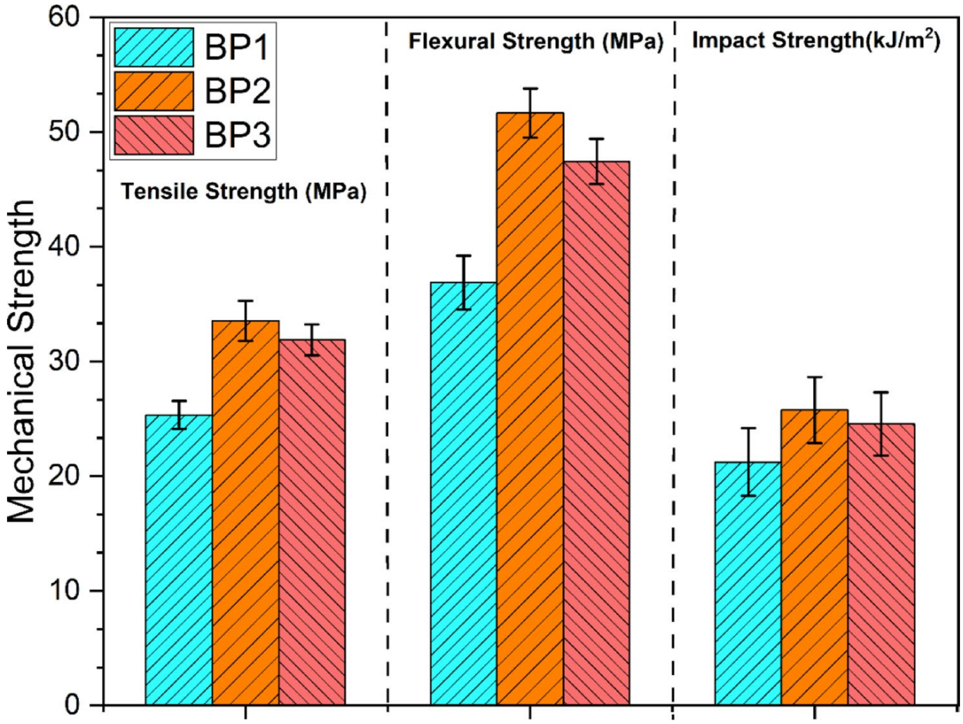

Fig. 4. Mechanical properties of BP1-BP3 composites; values are presented as mean ± standard deviation ($n = 3$).

kJ/m², followed by BP3 with 24.55 kJ/m², and BP1 with 21.23 kJ/m². The higher impact strength in BP2 is attributed to its optimal fiber configuration, in which the increased banana fiber content enhances energy absorption during sudden impacts. BP2 exhibited the highest average tensile and flexural strengths among the formulations studied in the present work. However, these values should be interpreted as representative of a balanced hybrid natural-fiber system, rather than as universally superior to previously reported banana-based composites. The main significance of BP2 lies in achieving the most favorable overall combination of mechanical behavior, thermal stability, moisture resistance, and machinability within the untreated banana–paddy straw epoxy compositions investigated here. Using BP3 with more paddy straw resulted in lower impact resistance, likely because paddy straw fibers are less tough than banana fibers. The lower impact strength of BP1 indicates that its reduced fiber content diminishes the composite's ability to dissipate impact energy. Overall, these findings highlight the importance of optimizing fiber content and composition to achieve high mechanical performance in hybrid fiber-reinforced composites.

SEM analysis of fractured surfaces

SEM micrographs of the fractured surfaces are essential and provide important information on fiber-matrix interactions and failure in banana-paddy straw hybrid composites. On the tensile fracture surfaces (Fig. 5a), BP1 showed clear evidence of poor interfacial adhesion, with many fiber pullouts, cavities, and an unbonded interface. The presence of slippery fiber surfaces and cavities indicates poor stress transmission between the matrix and the fiber, leading to premature failure. On the contrary, BP2 had fractured and embedded fibers, indicating better adhesion and enhanced interfacial bonding. The fact that fiber breakage rather than pullout occurred indicates that the increased banana fiber content in BP2 enabled effective load transfer, consistent with the higher tensile strength of this product. The same trends were also reported by Sumesh et al.[41] in ramie/flax hybrids, where SEM indicated that the greater the fiber-matrix compatibility, the smaller the pullout and the higher the tensile strength.

In the flexural fractured surfaces (Fig. 5b), BP1 exhibited a high degree of delamination, large cavities, and fiber pullout, indicating poor bonding under bending loads. These flaws limited the distribution of stress and resulted in premature crack propagation. On the other hand, BP2 had broken fibers in the resin and fewer holes, which showed better adhesion and energy absorption. The BP2 morphology implies it can withstand higher

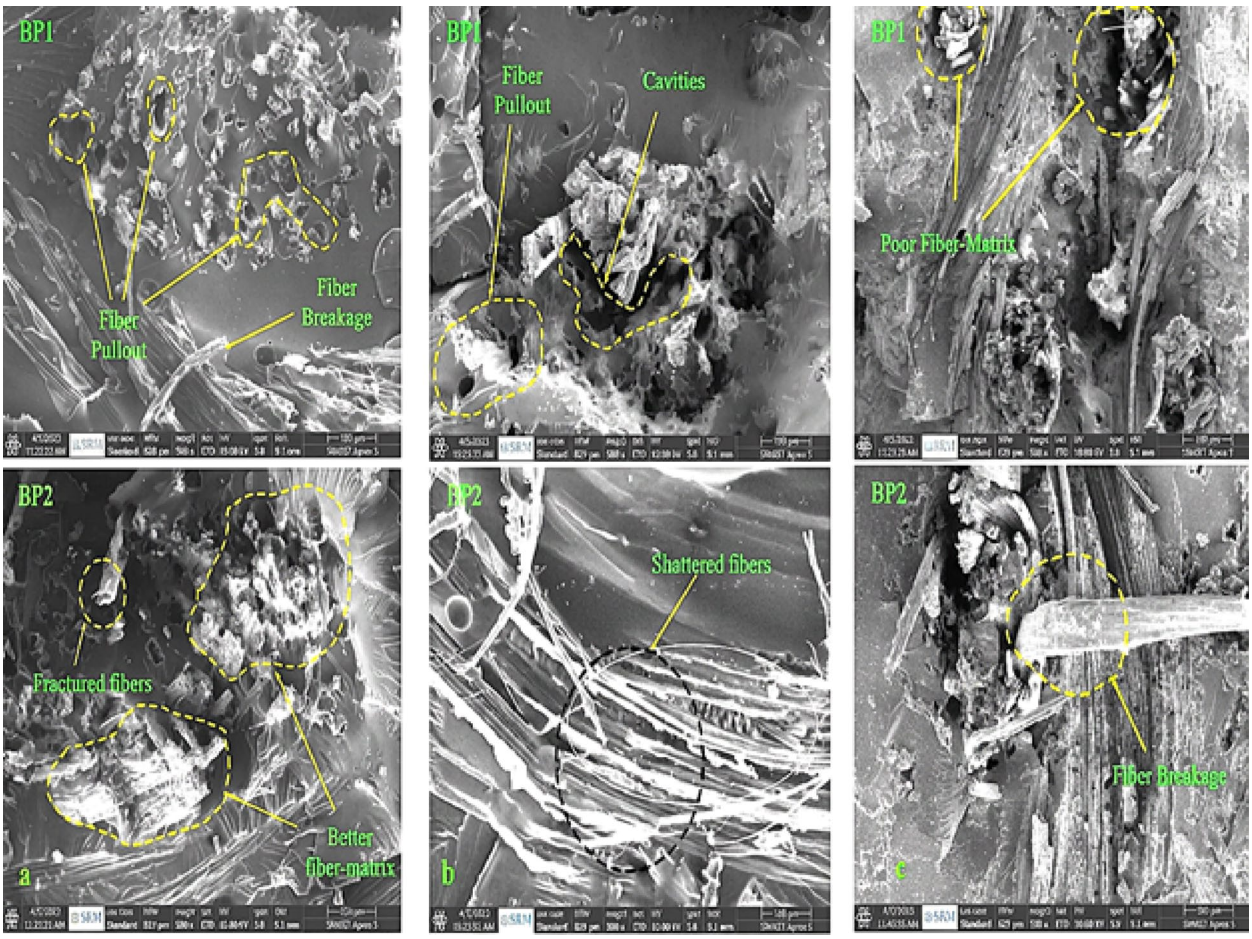

Fig. 5. (**a**) SEM analysis of Tensile test Fractured Surface (**b**) SEM analysis of Flexural test Fractured Surface (**c**) SEM analysis of Impact test Fractured Surface.

bending loads to failure, given its higher flexural strength. Similar observations have been reported for hemp/flax hybrid composites, where improved interfacial bonding resulted in reduced void content and cleaner fracture surfaces[42]. The SEM micrograph of the impact-fractured surfaces (Fig. 5c) shows clear differences between BP1 and BP2. The large-scale fiber pullout, cavities, and smooth surfaces in BP1 indicate poor fiber-matrix bond strength, resulting in most of the impact energy being dissipated by interfacial debonding. This is related to the weak bonding, which leads to low impact resistance in BP1. On the contrary, BP2 shows broken fibers in the matrix, coarse fractures, and localized cracks. All these observations indicate improved adhesion and multi-energy absorption, fiber breakage, matrix deformation, and microcracking, resulting in increased impact strength. Sumesh et al.[41] in ramie/flax systems, in which fractured fibers correlated with improved toughness, and Atmakuri et al.[42] were following suit by reporting similar results in hemp/flax hybrid. The high-energy absorption and impact resistance of BP2 are, therefore, justified by the superior fracture morphology of the material.

In all tests, BP1 exhibited poor adhesion, with fiber pullout, cavities, and delamination dominating its fracture surfaces. Conversely, BP2 showed better bonding, with fractured or broken fibers embedded in the matrix and fewer voids. This led to more efficient load transfer during tension, better stress distribution during bending, and superior energy absorption during impact. These microstructural observations qualitatively support the improved tensile, flexural, and impact behavior of BP2. However, since void content was not quantified, the SEM analysis should be interpreted as morphological evidence rather than a direct quantitative measure of consolidation quality. SEM fracture morphology was used in the present study as a qualitative tool to examine fiber pull-out, fiber breakage, matrix cracking, interfacial debonding, and void features in the fractured surfaces of BP1-BP3. The observations suggest that BP2 exhibited comparatively fewer visible voids, better fiber embedding, and stronger interfacial interaction than BP1 and BP3. However, since no quantitative fracture image analysis was performed, these SEM results should be interpreted as supporting morphological evidence rather than as a direct quantitative measure of fracture behavior or consolidation quality.

Thermal degradation behaviour

Figure 6a illustrates that the thermal degradation behavior of the hybrid composites BP1-BP3 is characterized by a multi-stage process typical of lignocellulosic fiber-reinforced epoxy composites. The initial stage (below 200 °C) involves the loss of absorbed water and volatile substances. The second stage (200–300 °C) corresponds to the breakdown of hemicellulose, while the peak degradation occurs between 300 and 400 °C due to cellulose decomposition. After 400 °C, decomposition mainly involves lignin and epoxy, leaving behind char residue. BP2 showed the highest stability, with the lowest weight loss rate and the greatest amount of remaining char compared to BP1 and BP3. This enhanced stability can be attributed to the increased cellulose-rich banana fiber content, which prolongs the decomposition process and enhances thermal resistance. Conversely, BP3 degraded earlier, consistent with the higher hemicellulose content in paddy straw, which degrades more easily. BP1 (Epoxy 70% + Banana 20% + Paddy straw 10%) demonstrated moderate stability, balanced between decreasing fiber content and increasing epoxy content.

To further clarify the thermal decomposition behavior of the hybrid composites, DTG curves (Fig. 6b) were also plotted alongside the TGA curves. The DTG profiles confirm the multistage degradation behavior of BP1-BP3. A minor degradation region below 200 °C is associated with the removal of absorbed moisture and volatile constituents. The intermediate region corresponds mainly to hemicellulose-related decomposition, while the dominant DTG peak in the range of approximately 300–400 °C is attributed to the major degradation of cellulose-rich constituents and the polymer matrix. Among the three laminates, BP2 exhibits a slightly delayed and lower peak degradation rate, indicating better thermal stability, whereas BP3 shows an earlier degradation trend, consistent with its relatively higher paddy straw content.

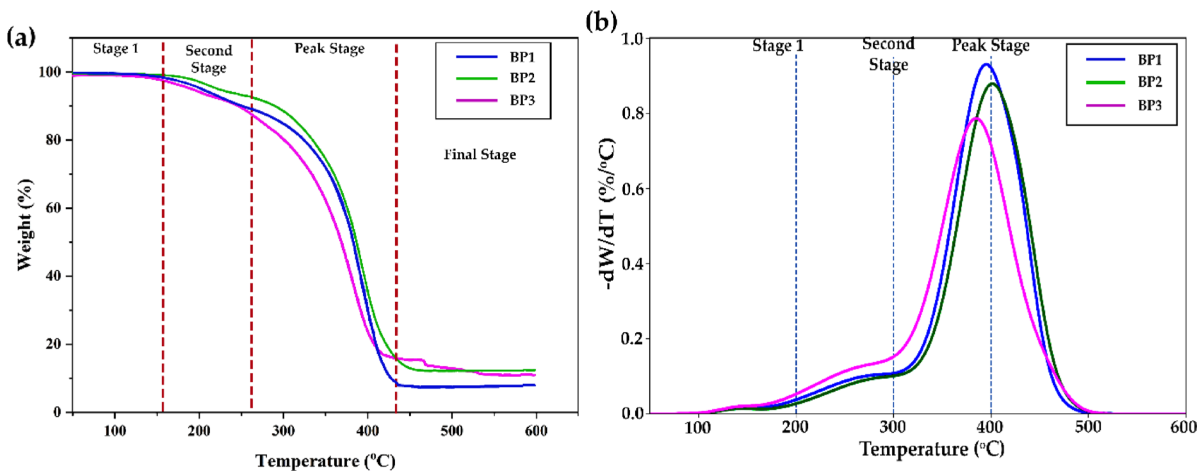

Fig. 6. (**a**) Thermogravimetric analysis (TGA) (**b**) Derivative thermogravimetric (DTG) curves of banana–paddy straw hybrid epoxy composites.

Sample	Tonset (°C)	Tmax (°C)	Residual mass/Char yield at 600 °C (%)
BP1	320	395	8.5
BP2	330	402	11.5
BP3	310	385	10.5

Table 2. Thermal degradation parameters of BP1-BP3 composites obtained from TGA/DTG curves.

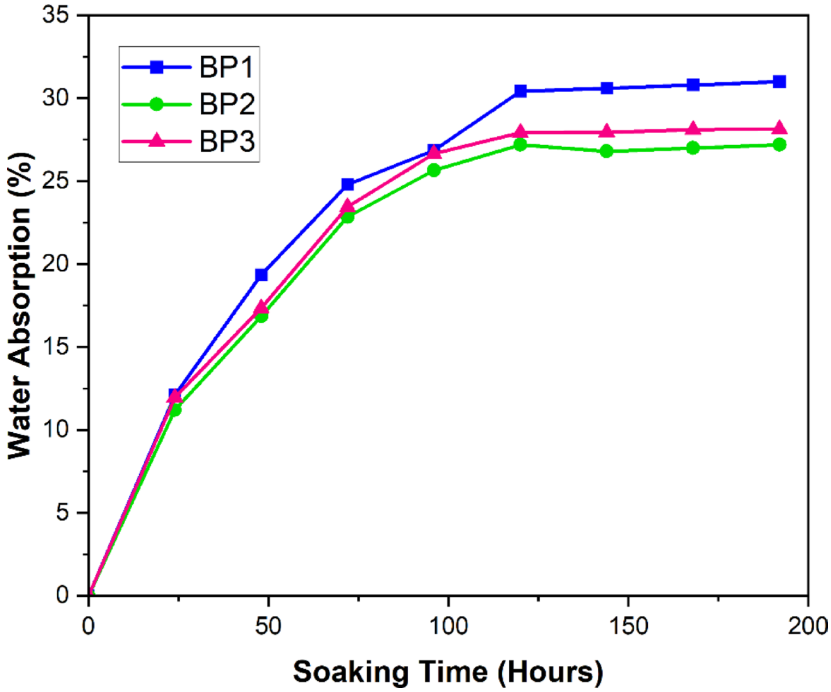

Fig. 7. Water absorption behaviour of banana–paddy straw hybrid epoxy composites.

To provide a more quantitative comparison of the thermal stability of the developed hybrid composites, the standard thermogravimetric parameters Tonset, Tmax, and residual mass (char yield) were estimated from the TGA/DTG curves, and the results are summarized in Table 2. Here, Tonset represents the onset temperature of the main degradation stage, Tmax corresponds to the temperature at the maximum degradation rate, as determined from the DTG peak, and residual mass indicates the char yield at 600 °C. Among the three laminates, BP2 showed the highest Tonset (330 °C), Tmax (402 °C), and residual mass (11.5%), indicating better thermal stability than BP1 and BP3. In comparison, BP3 exhibited the lowest Tonset (310 °C) and a lower Tmax (385 °C), while BP1 showed the lowest residual mass (~ 8.5%). These results are consistent with the TGA/DTG trends and confirm that BP2 exhibits greater thermal resistance, which may be attributed to its improved fiber-matrix interaction and more stable hybrid structure. These observations are in line with earlier studies. Balaji et al.[43] reported that banana fiber composites remained stable up to 220 °C before significant degradation, while Dua et al.[44] demonstrated that hybridization in Kevlar/natural fiber systems improved char yield and shifted the degradation temperature to higher values. The present results confirm that optimized fiber ratios, as in BP2, can achieve superior thermal stability, highlighting their suitability for applications requiring resistance to elevated temperatures.

Water absorption behaviour

The water uptake values of BP1–BP3 were approximately 27–31% (Fig. 7), which are relatively high for epoxy-based composites, but this behavior is not unexpected for untreated natural-fiber hybrid systems subjected to prolonged immersion. In the present study, water absorption increased rapidly during the first 50 h and then slowed, reaching near-equilibrium at around 150 h, indicating moisture diffusion through both the fiber-rich regions and the fiber–matrix interfacial microvoids. This behavior is consistent with the lignocellulosic nature of banana and paddy straw fibers, whose cellulose- and hemicellulose-rich constituents promote hydrophilicity and water retention. Among the three laminates, BP1 showed the highest uptake (~ 31%), suggesting comparatively poorer interfacial sealing and more accessible diffusion pathways. BP2 exhibited the lowest uptake (~ 27%), which is attributed to better fiber packing and stronger interfacial bonding that restricted water ingress. BP3 showed intermediate absorption (~ 28%) and a slightly higher uptake relative to BP2, associated with the increased paddy straw content and the greater hydrophilic contribution of hemicellulosic constituents. A similar trend has been reported in earlier banana-fiber epoxy studies, where alkali treatment and alumina filler reduced water absorption to about 24% by improving interfacial integrity and resistance to water penetration. Thus, although the absolute water-uptake values are high, the relative trend among BP1–BP3 still confirms that BP2 has the best moisture resistance among the tested formulations.

These results are consistent with prior reports. Praveena et al.[45] observed that pineapple leaf fiber composites displayed increasing absorption with fiber content due to cellulose-driven hydrophilicity. Similarly, Vinoth et al.[23] found that paddy straw hybrid laminates absorbed more moisture when higher fiber fractions and voids were present. Overall, while natural fibers inherently raise water uptake, the optimized BP2 composition demonstrates improved resistance, balancing reinforcement and durability against moisture ingress.

Machining characteristics

BP2 exhibited the highest mechanical strength among all fabricated laminates, which was one of the reasons for choosing it for machinability testing under various process parameters. AWJM, known for its high accuracy and ability to machine composite structures without heat damage, is a suitable method for studying the machinability of BP2. The study analyzes the effects of key AWJM parameters, including abrasive flow rate, traverse speed, and standoff distance, on output responses such as surface roughness and kerf angle. The goal of the present work is to optimize the machining parameters for BP2 to minimize errors, achieve satisfactory dimensional accuracy, and obtain a good surface finish, thereby demonstrating BP2's potential for advanced technical applications.

Design of experiments

Experiments were designed using a 27-run, three-factor, three-level design implemented in Design-Expert 13 under a user-defined RSM framework. The three AWJM input parameters considered were AFR, TS, and SoD, each studied at three levels. The L27 design was selected because it provided a structured dataset suitable for estimating main effects, two-factor interactions, and quadratic terms required for second-order RSM modeling of surface roughness (SR) and kerf angle (Kf). Thus, the design enabled efficient development of quadratic response models while keeping the number of experiments manageable. The experimental combinations and corresponding response values are listed in Supplementary Table 2.

Artificial neural networks

Layered networks called ANNs have an input layer, hidden layers, and an output layer that resemble the brain's structure[46]. During training, an ANN's ability to recognize intricate patterns and correlations in data is enhanced by adjusting link weights. They are beneficial for jobs involving pattern recognition, regression, and classification because they can automatically extract features from unprocessed data. However, ANNs also have drawbacks, such as the need for large amounts of labeled data, the risk of overfitting, and issues with interpretability[47,48]. This study uses Python to enhance a feedforward neural network for regression tasks, including predicting AWJM surface roughness and kerf angle.

<u>Model architecture</u> This research addresses a challenge in AWJM, a widely used material-cutting process across various industries. The primary objective is forecasting two critical factors: 'SR' and 'Kf'. Predicting these results helps you monitor and control the AWJM process in real time. In turn, this helps to improve the process, making it work better, waste less, and produce better products. It's also possible to optimize processes with predictive capabilities, helping engineers and workers achieve better results. TensorFlow and Keras are used to build the neural network topology. The code sets up a custom method called create_model that can be used to make a Sequential model (2) with any number of hidden layers and neurons.

$$Model\ Output = f_n(\ldots f_2(f_1(Input))\ldots) \tag{2}$$

where f_n represents the activation function applied in layer n, and the parameters (weights and biases) are learned during the training process. The choice of a flexible architecture allows for experimentation with different model complexities to capture intricate patterns in the data. Regression tasks are performed by a single neuron in the output layer, while the hidden layers use the Rectified Linear Unit (ReLU) activation function (3).

$$f_{\mathrm{Re}\,LU}(x) = \max(0, x) \tag{3}$$
$$f_{Linear}(x) = x$$

A multi-layer perceptron (MLP) architecture is appropriate for this regression task, as it can capture complex relationships within the input features to predict the continuous target variables.

<u>Hyperparameter tuning</u> For hyperparameter tuning of the ANN models, GridSearchCV was used to systematically optimize the model architecture. The search space included the number of hidden layers and the number of neurons per layer, and the prediction error was minimized using mean squared error (MSE) during the grid search. The neuron range was set to 2–10, and the explored architectures included single-, two-, and three-hidden-layer configurations. To minimize prediction errors, the study used mean squared error (4) as the scoring metric during grid search. This helps identify the optimal hyperparameter combinations so the neural network can make accurate predictions.

$$MSE = \frac{1}{n}\sum{}_{i=1}^{n}(Actual_i - \mathrm{Pr}\,edicted_i)^2 \tag{4}$$

where n is the quantity of information. The neuron_range defines a size range of two to ten neurons.

neuron_range = range(2, 10).

param_grid = {.

'keras__hidden_layer_sizes': [(size,) for size in neuron_range] + [(size, size) for size in neuron_range] + [(size, size, size) for size in neuron_range],

}

Within the param_grid dictionary, various combinations of hidden layer sizes are listed for exploration during the grid search. The code generates tuples representing distinct neural network architectures for each size specified in the neuron_range. These designs cover single-layer, two-layer, and three-layer layouts. Through methodical investigation, many network topologies can be thoroughly searched, enabling the determination of which architecture is best suited for the task during the hyperparameter tuning phase. (Supplementary data)

In addition to the architectural search, the ANN training procedure was carried out using fixed training settings, which are now reported explicitly for reproducibility. These include the learning rate, the regularization strategy adopted to reduce overfitting, and the stopping criterion used to terminate training. The training configuration consisted of the Adam optimizer with a learning rate of 0.5, batch normalization, and a fixed stopping criterion of 1000 training epochs.These settings were kept constant while the hidden-layer architecture was optimized through grid search.

This systematic hyperparameter tuning helps identify the combination of hyperparameters that yields the best predictive performance, thereby enhancing the model's generalization capabilities.

$$MAE = \frac{1}{n}\sum {}_{i=1}^{n}(Actual_i - \Pr edicted_i) \tag{5}$$

$$R^2 = 1 - \frac{\sum \ {}_{i\,=\,1}^{\ n}\ (Actual_i - \Pr edicted_i)^2}{\sum \ {}_{i\,=\,1}^{\ n}\ (Actual_i - Mean\,(Actual))^2} \tag{6}$$

The algorithm evaluates the improved models using a validation set after hyperparameter adjustment. Measures of the models' accuracy and quality of fit include Mean Absolute Error (MAE) (5) and R^2 (6) scores. For SR, the architecture 3–4-4-1 (three input nodes, two hidden layers with four neurons each, and one output node) was identified as optimal, achieving an R^2 value of 0.965 and an MAE of 0.13. For Kf, the architecture 3–6-5-5–1 (three input nodes, three hidden layers with six, five, and five neurons, respectively, and one output node) demonstrated superior performance, achieving an R^2 value of 0.987 and an MAE of 0.08. To get this final design, the neural network's hyperparameters were carefully adjusted using a rigorous optimization procedure (Fig. 8). The optimization process included systematic hyperparameter tuning, flexible neural network construction, and in-depth interpretation of results to provide a holistic solution to a significant manufacturing challenge. This method improves predictive modeling within the AWJM framework.

<u>The function of training and loss</u> The input variables were standardized using StandardScaler, and the network was trained using the Adam optimizer for 1000 epochs with a batch size of 4. The dataset consisted of 135 data points, of which 80% (108 points) were used for training, and the remaining 20% for testing/validation. Model performance and potential overfitting were monitored using training-validation loss curves and MAE and R^2 values.

With 135 data points, 80% (108) were allocated to training, while the remaining 20% (27) were used for testing and validation. Hyperparameters, including the number of neurons and layers, were optimized via grid search. Figure 9 illustrates the training and validation loss curve, providing insights into the model's performance over the training epochs. It's important to note that surface roughness and kerf angle models exhibit nearly identical mean absolute error and R-squared values. This similarity in performance metrics between the two models contributes to the similarity of their training and validation curves. However, it's crucial to acknowledge that although both models initially exhibit variation between the training and validation stages, merging these curves in the later stages indicates convergence in performance. This agreement indicates that the models can properly describe the interactions among input variables and machinability outputs, and can predict responses with confidence and reliability[49]. This plot is useful for estimating the model's ability to learn the data and for identifying when you may need to adjust the model to avoid overfitting and underfitting. The fact that the training and validation loss curves of both models are closely superimposed demonstrates the increased precision of this predictive model. This coincidence indicates that the models generalize well to the test data and can be useful for predicting features associated with AWJM.

<u>Model performance</u> The model's predictive accuracy for SR and Kf is assessed on the validation set using R-squared (R^2) and MAE as evaluation metrics. MAE determines the mean difference between expected and actual values, and the degree to which the input characteristics can explain the variation in the target variable is determined by R^2. Following training, the loss history for each prediction model is presented using Matplotlib, facilitating analysis of convergence and identifying potential overfitting. Figure 10 illustrates the model's performance, demonstrating its effectiveness in predicting wear characteristics. For Surface Roughness (Fig. 10a), the model achieves a remarkably low MAE of 0.13. This small MAE, indicating an average absolute deviation of only 0.13 units from the actual values, implies accurate forecasts. The model also demonstrates substantial explana-

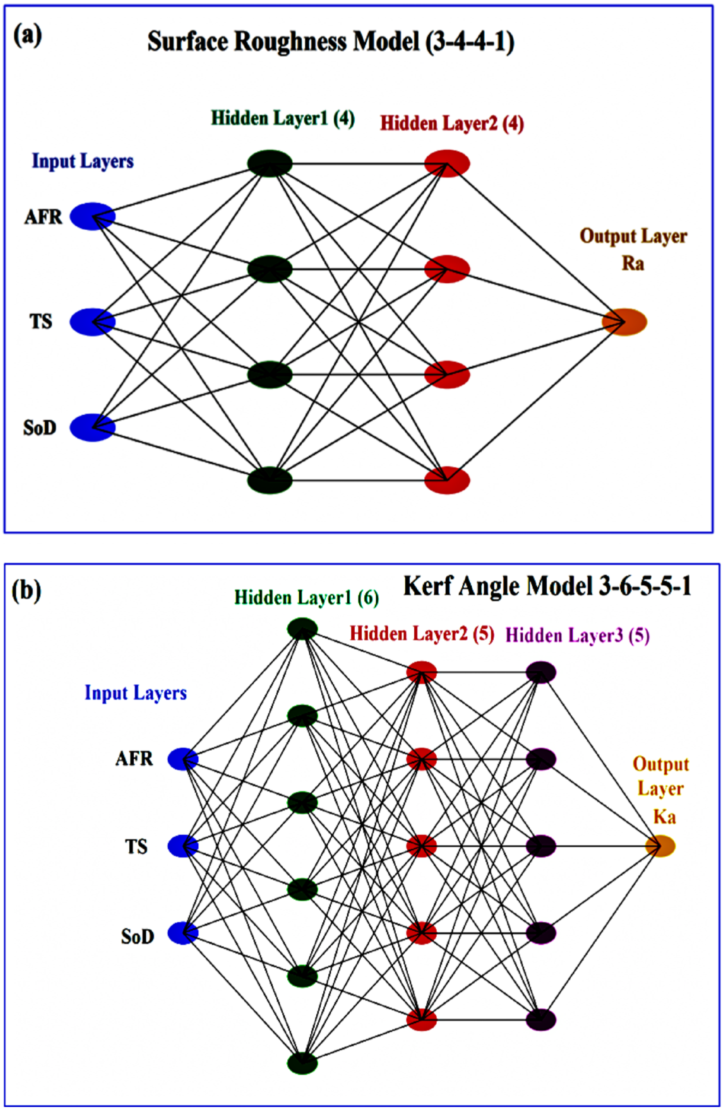

Fig. 8. ANN Architecture for (**a**) Surface Roughness model, (**b**) Kerf Angle model.

tory power, as evidenced by an impressive R-squared value of 0.965. This strong R^2 indicates that 96.5% of the observed variance in Surface Roughness (SR) is explained by the input characteristics.

As with the Kerf Angle (Fig. 10b), the model's low MAE of 0.08 indicates that the average absolute difference between forecasts and actual values is 0.08 units, suggesting the model is reliable. The model's exceptional R^2 score of 0.987 further highlights its competence. With an R^2 of 98.7%, the model explains 98.7% of the variability in the Kerf Angle as a function of the input characteristics, demonstrating an outstanding ability to identify meaningful patterns within the data.

The density curves in Fig. 11 for both SR and Kf models visually represent the distribution of actual versus predicted values, providing insight into the accuracy and reliability of the ANN models developed in this study. In Fig. 11a, which shows the density of Surface Roughness predictions, the blue curve represents the actual values, while the orange curve corresponds to the predicted values. The close correspondence between the two curves indicates that the model's prediction accuracy is high. The good agreement at the peak and tails indicates that the distribution of actual surface roughness values is well modeled, resulting in minimal prediction errors. Similarly, in Fig. 11b, a density plot of the Kerf Angle predictions shows a high degree of overlap between the actual (blue) and predicted (orange) curves. This provides additional evidence supporting the model's ability to predict the Kerf Angle from input features.

The near overlap of the density curves for Kerf Angle, as with Surface Roughness, indicates the model's strong predictive power. Visual continuity between the actual and predicted distributions for both Surface Roughness and Kerf Angle indicates good performance of the ANN, suggesting that the models are well-calibrated and generalize well to unseen data. Based on this density analysis, it is concluded that the trained models can reliably predict AWJM characteristics, aiding process optimization and improving manufacturing outcomes. The evaluation of the ANN model's forecasting performance is further illustrated in Fig. 12, which also provides

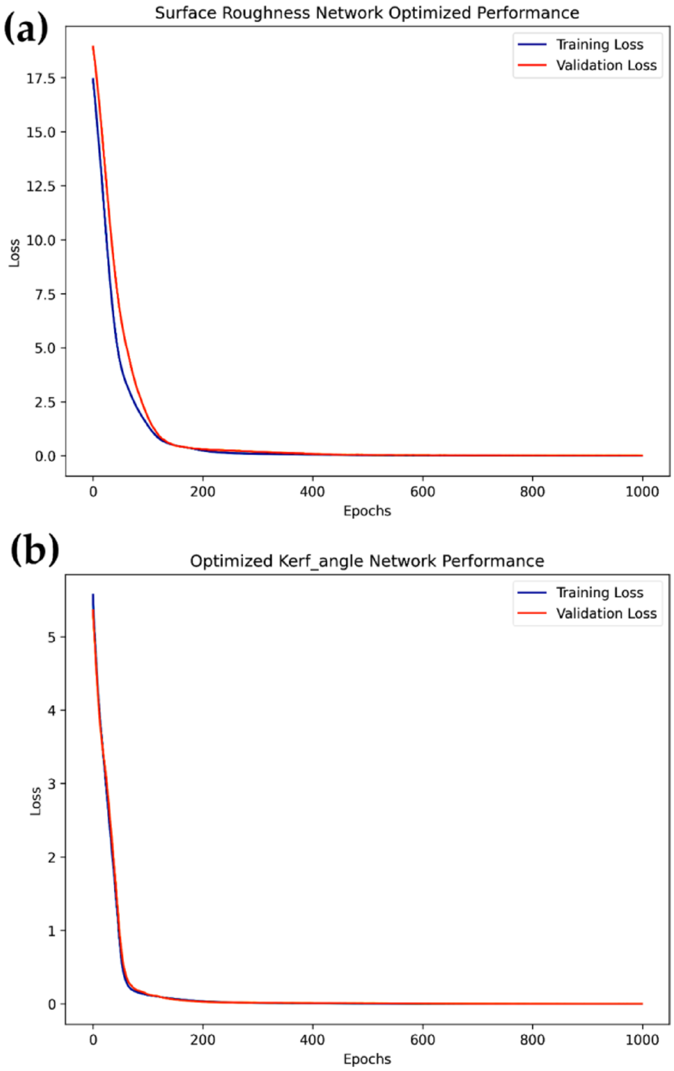

Fig. 9. Curve for Training and Validation Loss (**a**) Ra (**b**) Ka model.

online analysis of additional design matrices and compares actual and predicted values for Surface Roughness (SR) and Kerf Angle (Kf). In the heatmaps, the x-axis represents the sample index, and the y-axis displays actual and predicted values. The values of the proportional infinity plotted on the maps are indicated by color gradients, from dark to light; darker colors correspond to lower values, while brighter colors indicate higher values.

The details of the Surface Roughness model (Fig. 12a) are as follows: each column corresponds to a specific sample index; the upper half of each column shows the absolute value, and the bottom half shows the expected value. The clusters of light blue circles and dark blue triangles indicate that the actual and predicted values from the model are nearly color-matched, suggesting the model's predictions are quite accurate and reasonable. Similarly, the consistent color matching between the top and bottom halves of each column in the Kerf Angle model heatmap (Fig. 12b) demonstrates a strong correlation between the real and predicted outputs. These heat maps confirm the ANN models' reliability in predicting efficient surface roughness and kerf angle, thereby enhancing their credibility for optimizing the AWJM process. The small clusters of differing colors between actual and predicted values across various sample indices show that the model has effectively captured the true data patterns, making its predictions accurate and trustworthy. Higher R^2 scores indicate that these models successfully capture the primary variability in each parameter, reflecting their accuracy and precision in defining the AWJM characteristics of the hybrid biocomposite Paddy straw-Banana. When advanced machine learning techniques are properly applied, such models can deepen our understanding of material properties and even revolutionize material optimization across various applications.

To further evaluate the generalization capability of the developed ANN models, 5-fold cross-validation was performed for both the surface roughness (SR) and kerf angle (Kf) models. The cross-validation results are presented in Fig. 13, where the mean absolute error (MAE) obtained for each fold is shown. For the SR model, the average MAE across the five folds was 0.0994, indicating good predictive consistency. For the Kf model, the average MAE was 0.9525. Although some variation was observed among individual folds, the overall results support the reliability of the ANN predictions within the investigated AWJM parameter range. These findings

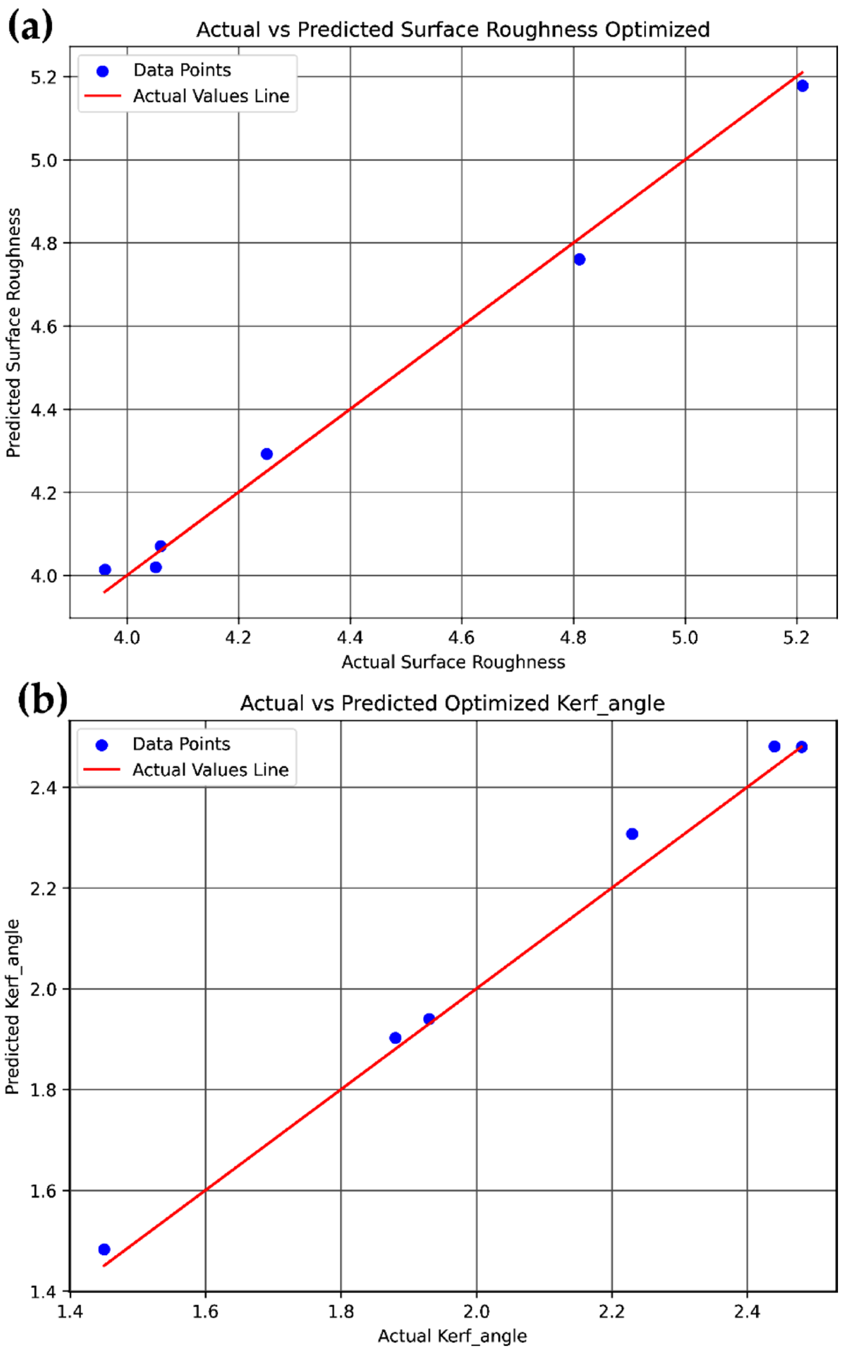

Fig. 10. The model's predictive performance (**a**) SR (**b**) Kf.

further strengthen the ANN validation in addition to the train-test split analysis and the comparative validation with RSM.

Ang, J.Y. et al.[50] have developed an ANN model to estimate the initiation of failure in glass fiber-reinforced epoxy composite pipes under multiaxial loading. With a balanced split of 15% for each, 70% of the data was reserved for training and 30% for testing and validation. The authors of the present study have surpassed the model's accuracy on their data. In contrast, Jayabla et al.[36] used an ANN with feedforward backpropagation to predict the mechanical properties of coir fiber, with batch sizes of 5 and 1000 epochs. The average absolute error percentages for the tensile, flexural, and impact strength models were 0.98, 0.86, and 0.44, respectively, as determined by their ANN models. In this project, this work tunes a feedforward neural network for regression using Python and Grid Search for hyperparameter tuning. The results demonstrate the reliability of the ANN model's predictions based on the observed values, with considerably low mean absolute errors (0.13 and 0.08).

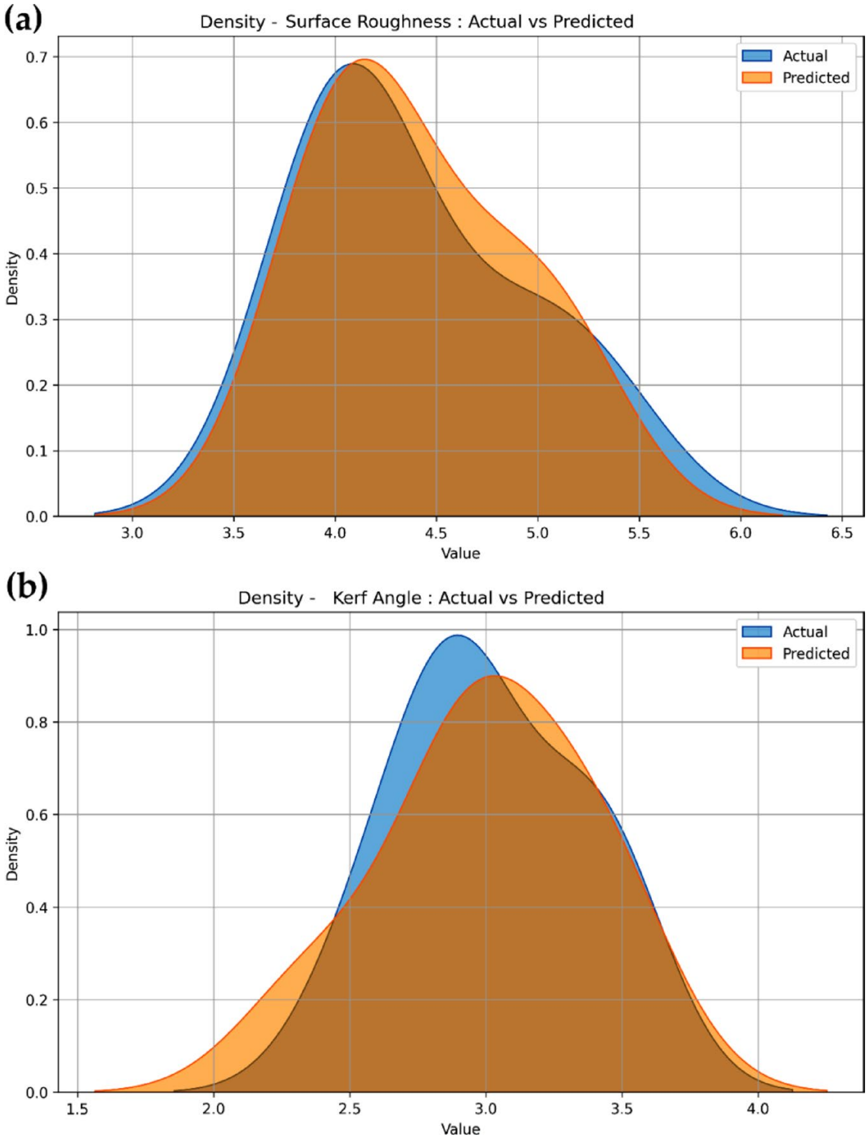

Fig. 11. Density curve for (**a**) SR (**b**) Kf model.

Response surface methodology

Regression models An ANOVA analysis was performed to examine the models, terms, and their interactions. The models were highly statistically significant, with p-values less than 0.0001. Additionally, the models proved adequate, as shown by diagnostic tests such as lack-of-fit and residual analyses. These validations provide a solid basis for optimizing and ensuring the consistency of the regression models when predicting machining responses. Quadratic regression models were developed using Design-Expert 13 to correlate the AWJM input parameters with the machining responses. The models are expressed in terms of the actual process variables, namely abrasive flow rate (AFR, g/min), traverse speed (TS, mm/min), and standoff distance (SoD, mm). The predicted response variables are surface roughness (SR, µm) and kerf angle (Kf, °). The complete second-order regression equations with numerical coefficients are given in Eqs. (7) and (8)[51]. The SR and Kf models exhibited high R^2 values (0.9830 and 0.989), indicating robust understanding and reliable forecasting based on the predefined process variables.

$$\begin{aligned} SR = {} & 7.88315 + (0.003372 \times AFR) - (0.0211 \times TS) - (0.4233 \times SoD) \\ & - \left(1.67 \times 10^{-5} \times AFR \times TS\right) + (0.00025 \times AFR \times SoD) + (0.000317 \times TS \times SoD) \\ & - \left(0.000013 \times AFR^2\right) + \left(0.000045 \times TS^2\right) - \left(0.022778 \times SoD^2\right) \end{aligned} \tag{7}$$

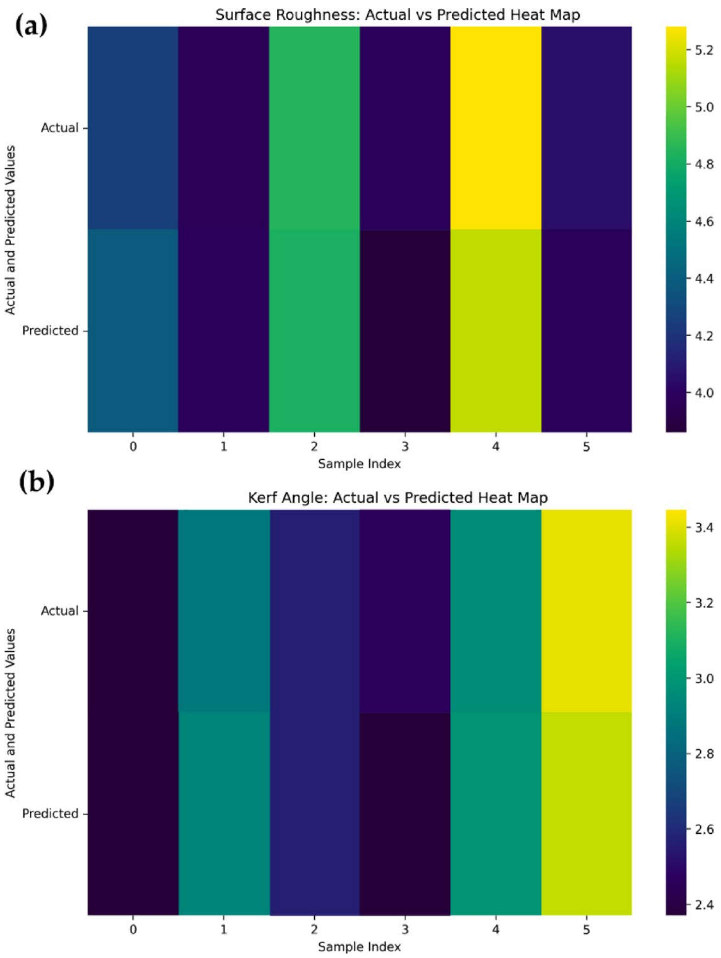

Fig. 12. Heatmap plot for both (**a**) SR and (**b**) Kf Model.

$$\begin{aligned} KF = {} & 3.66361 - (0.002769 \times AFR) - (0.0072 \times TS) - (0.145833 \times SoD) \\ & - \left(1.5 \times 10^{-6} \times AFR \times TS\right) + (0.000175 \times AFR \times SoD) + (0.000183 \times TS \times SoD) \\ & - \left(1.67 \times 10^{-7} \times AFR^2\right) + \left(0.00001 \times TS^2\right) - \left(0.085 \times SoD^2\right) \end{aligned} \tag{8}$$

Surface roughness model (SR) The ANOVA results in the Supplementary Table 3 summarizes the statistical results for the response model, indicating that the overall model is highly significant (p-value < 0.0001). This suggests that the model is a good fit for the data. AFR (A), TS (B), and SoD (C) collectively explain 98.67% of the observed variation, with significant contributions to the model. Based on the ANOVA results presented in Supplementary Table 3, the percentage contribution of each factor indicates that Standoff Distance (C) is the most influential parameter (52%), followed by Abrasive Flow Rate (A) (42%) and Traverse Speed (B) (4%). Interaction and quadratic terms, while statistically significant, have relatively minor contributions compared to the main effects. The residuals have a low mean-squared error, indicating that the model accounts for a substantial portion of the response variability. The R^2 is 0.9867, demonstrating that the model explains about 98.67% of the total variability. The adjusted R^2 is 0.9796, and the predicted R^2 is 0.9640, affirming the model's prediction reliability. In summary, the ANOVA table confirms the model's significance, identifies influential factors, and provides key metrics for assessing its goodness-of-fit and predictive capability.

Figure 14a shows a 3D surface plot of AFR, TS, and SR, demonstrating that higher AFR results in better dispersion of abrasive particles and promotes a more uniform processing action, thereby reducing surface roughness. Surface roughness decreases slightly as the traverse speed increases from 150 mm/min to 200 mm/min, then rises again as the speed increases further due to resonant frequencies and vibrations that affect surface quality. Figure 14b shows that, within the tested range, increasing SoD was associated with a reduction in the measured surface roughness (SR). However, this should not be interpreted as an overall improvement in cut quality. A larger SoD causes the jet to lose coherence and spread before reaching the workpiece, reducing local cutting aggressiveness and potentially yielding a smoother, averaged surface profile. At the same time, this jet divergence reduces dimensional precision, resulting in a wider cut and a higher kerf angle. Therefore, the effect of SoD on SR must be interpreted alongside kerf quality rather than as an independent indicator of better machining performance.

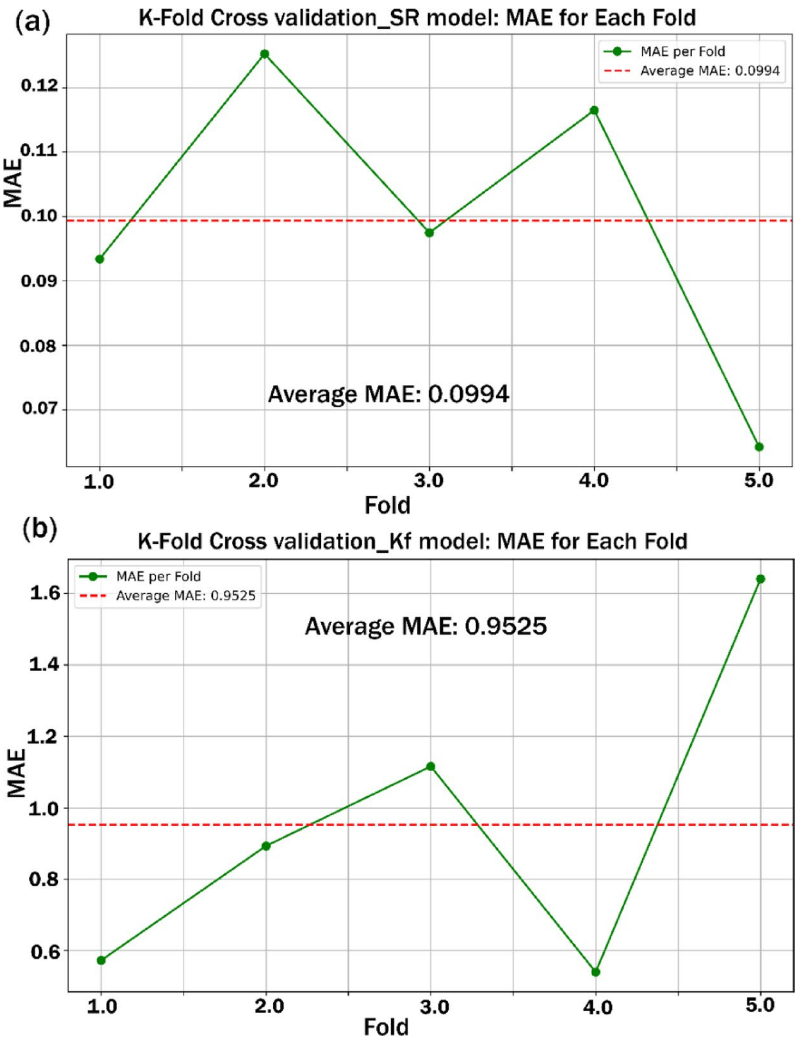

Fig. 13. Results of 5-fold cross-validation for the ANN models (**a**) SR (**b**) Kf model.

The interaction between TS and SoD significantly influences SR in AWJM, as illustrated in Fig. 14c. For each set of traverse speed, an increase in SoD from 2 mm to 4 mm generally corresponds with a decrease in surface roughness. This reduction becomes particularly noticeable at higher standoff distances (3 mm and 4 mm) as the traverse speed increases. The observed decrease in SR at larger standoff distances within the tested range indicates a smoother measured surface profile, but not necessarily superior overall cut quality, since higher SoD also promotes jet divergence and kerf deterioration.

Kerf angle model (Kf) The ANOVA findings are shown in Supplementary Table 4, which provides a statistical analysis of the experimental data and highlights the importance of the different variables and their interactions in predicting the response variable. With a p-value less than 0.0001, a sum of squares (SS) of 3.63, and 9 degrees of freedom (df), the model is highly significant and accounts for 99.0% of the total variability. AFR, TS, and SoD are the three most critical individual parameters, accounting for 47%, 13%, and 37% of the model, respectively. Interaction terms (AB, AC, BC) make negligible contributions, while the quadratic effect of SoD (C^2) is statistically significant, accounting for 1%. The residuals, representing unexplained variability, have an SS of 0.0376. The total sum of squares (Cor Total SS) is 3.67, encompassing both the model and residual variability. The standard deviation is 0.0470, and the coefficient of determination (R^2) is 0.9897, indicating a high proportion of variability explained by the model. The adjusted R^2 (0.9843), predicted R^2 (0.9698), and Adequacy Precision (52.3564) further affirm the model's robustness and its ability to accurately predict the response variable.

The analysis of the interaction between AFR and TS reveals a significant relationship with Kf in AWJM (Fig. 15a). There is a clear pattern that indicates that the kerf angle decreases noticeably as the AFR rises. Higher AFR is thought to be responsible for the additional abrasive particles it delivers to the jet, improving penetration capabilities and producing a more accurate cutting path. The Kf is also influenced by traverse speed, where a rise in traverse speed is correlated with a commensurate decrease in kerf angle. The dependence of these factors on maximizing machining accuracy is highlighted by the minimal kerf angle observed at an AFR of 400 g/min and a TS of 250 mm/min.

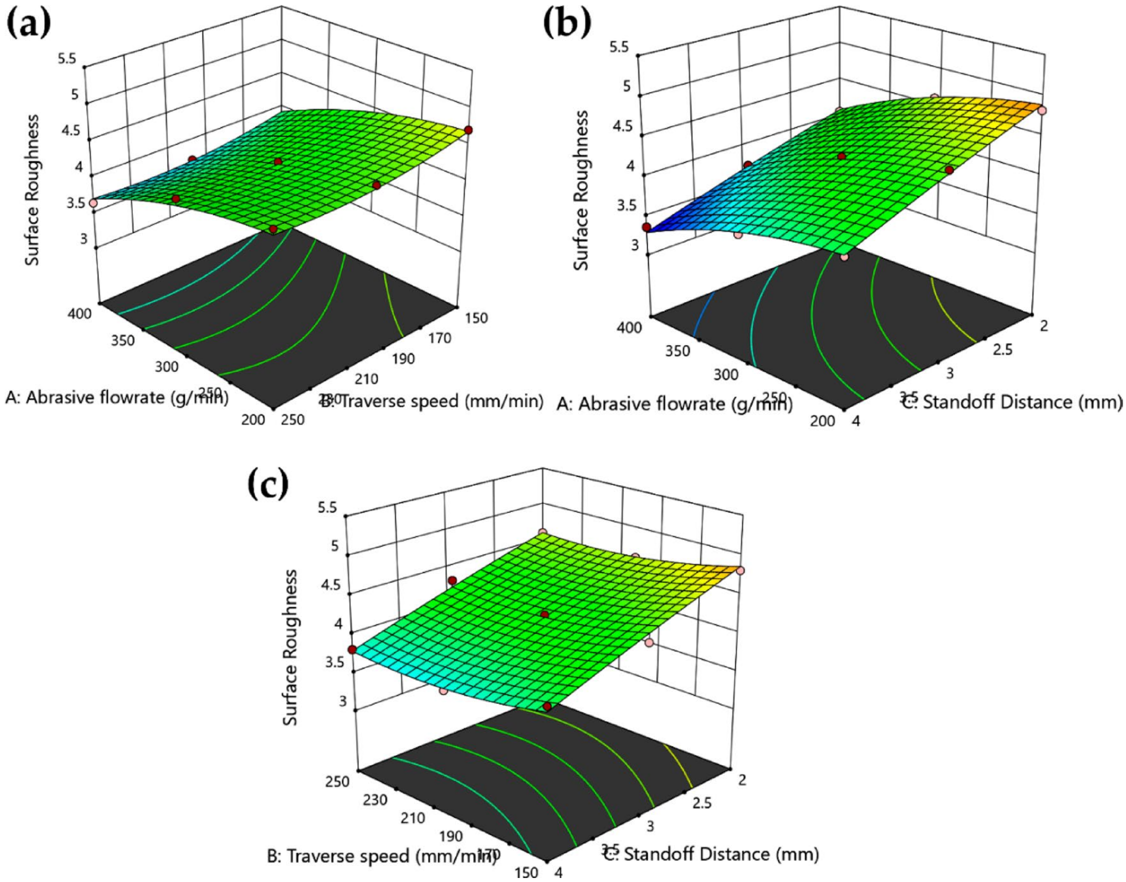

Fig. 14. (**a**-**c**) 3D surface plot – surface roughness model.

A substantial association is evident in Fig. 15b, where an increase in Kf is correlated with an increase in SoD. The water jet's innate propensity to diverge as the SoD rises explains this link. A broader cutting path is produced when the water jet expands, increasing the kerf angle. The abrasive particles impact a larger surface area because the jet tends to spread, resulting in a wider cutting path. Consequently, a larger kerf angle is formed due to this broader impact region. On the other hand, the analysis of Fig. 15c reveals a notable absence of substantial variation in Kf with respect to the relationship between TS and SoD. This observation suggests that when both TS and SoD are varied simultaneously, their combined effect on the kerf angle is minimal. The findings emphasize the intricate dynamics of SoD in influencing the Kf. In contrast, the simultaneous variation of TS and SoD does not produce a pronounced effect on the kerf angle in abrasive waterjet machining.

Input parameters optimization The present study optimized AWJM of banana–paddy straw hybrid composites and identified optimal parameters (AFR: 400 g/min, TS: 250 mm/min, SoD: 3 mm) that minimized surface roughness (SR = 3.60 μm) and kerf angle (Kf = 1.56°). To contextualize these findings, it is important to compare AWJM performance with other reported machining processes for natural fiber composites. Conventional drilling and milling often result in severe delamination, fiber pull-out, and high tool wear due to the heterogeneous, abrasive nature of fibers. A comparison of different machining processes for Banana and other natural fiber polymer composites is presented in Supplementary Table 5.

The AWJM trends observed in the present study are broadly consistent with recent studies on natural-fiber-reinforced composites. In the hybrid rice straw/Furcraea foetida composite studied by Madival et al.[30], the traverse speed showed the highest contribution to material removal rate and kerf-width responses, while the interaction between fiber concentration and traverse speed most strongly influenced kerf taper. The same study also noted that increases in standoff distance and traverse speed can degrade surface quality due to jet spreading, kinetic energy loss, and reduced cutting stability. Likewise, Kalirasu et al.[52] reported that AWJM output quality in banana/polyester composites is highly sensitive to the selected cutting parameters, especially those governing jet conditions and kerf formation. More recently, Kumar and Dinesh Babu[53], in a PLA/bamboo/clay hybrid system, reported that traverse rate was the most influential factor, followed by abrasive feed rate, while standoff distance had a comparatively lower contribution; they also observed that kerf angle increased with standoff distance, whereas material removal rate increased with traverse rate. In comparison, the present banana–paddy straw hybrid epoxy composite also showed strong sensitivity to AFR, TS, and SoD, but the optimum condition occurred at AFR = 400 g/min, TS = 250 mm/min, and SoD = 3 mm, indicating that the exact balance between surface finish and kerf quality is material-dependent. Thus, the present results support the broader AWJM

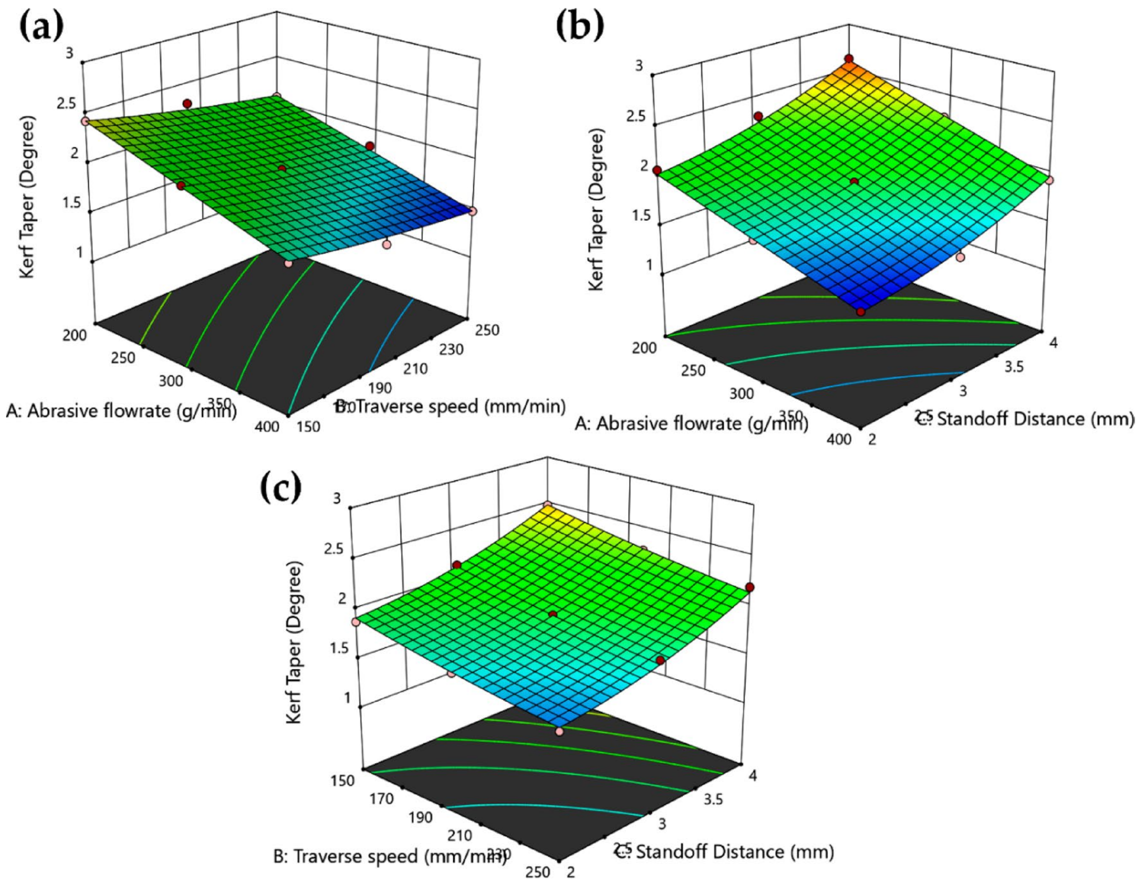

Fig. 15. (**a**-**c**) 3D surface plot - Kerf angle model.

literature while also highlighting the distinct machining response of the developed banana–paddy straw hybrid composite.

Validation of ANN and RSM

Comparing actual SR and Kf values with expected ones is a practical way to predict the performance of RSM and ANN models. These models forecast SR and Kf under experimental conditions that include fluctuations in AFR, TS, and SoD. The error percentage is calculated by comparing the actual values from trials with the predicted ones from RSM and ANN to evaluate model performance. Calculating the average absolute error percentages for SR and Kf shows that, in general, the ANN model has a lower absolute error than the RSM model for both responses. This indicates that the ANN model achieves higher predictive accuracy in AWJM, offering valuable insights for optimizing machining settings to enhance surface quality and precision. Supplementary Table 6 serves as a comprehensive validation tool in abrasive waterjet machining, illustrating how well these modeling methods capture the complex relationships between process factors and surface characteristics.

The ANN model outperformed the RSM model in terms of prediction accuracy and average absolute error, as demonstrated in the comparison study. This improved performance is attributed to the ANN's adaptable structure, hyperparameter tuning with GridSearchCV, and its capacity to handle complex, non-linear relationships. The predictability, reliability, and validation of the ANN models for SR and Kf were confirmed with experimental data. The ANN achieved superior results compared to RSM, with MAEs of 0.13 and 0.08, and R^2s of 0.965 and 0.987 for SR and Kf, respectively. This indicates that the ANN effectively predicts machining outcomes across various scenarios, making it a valuable tool for optimizing AWJM performance. Moreover, this research enhances the understanding of the complex behavior of AWJM. It offers recommendations for engineers and practitioners, especially those aiming to identify minimum acceptable cutting conditions to improve surface quality and finish. Finally, the developed predictive models serve as useful decision-making tools for selecting optimal parameters and making informed choices in abrasive water jet machining. Extrapolation tests and experimental data validation assessed the ANN model's robustness to variations in input parameters. The model showed strong predictive capability for both SR and Kf, with good reliability across the experimental range. However, predictions outside the training data were less accurate, highlighting the need to expand the training dataset to improve the model's reliability across a wider range of parameters.

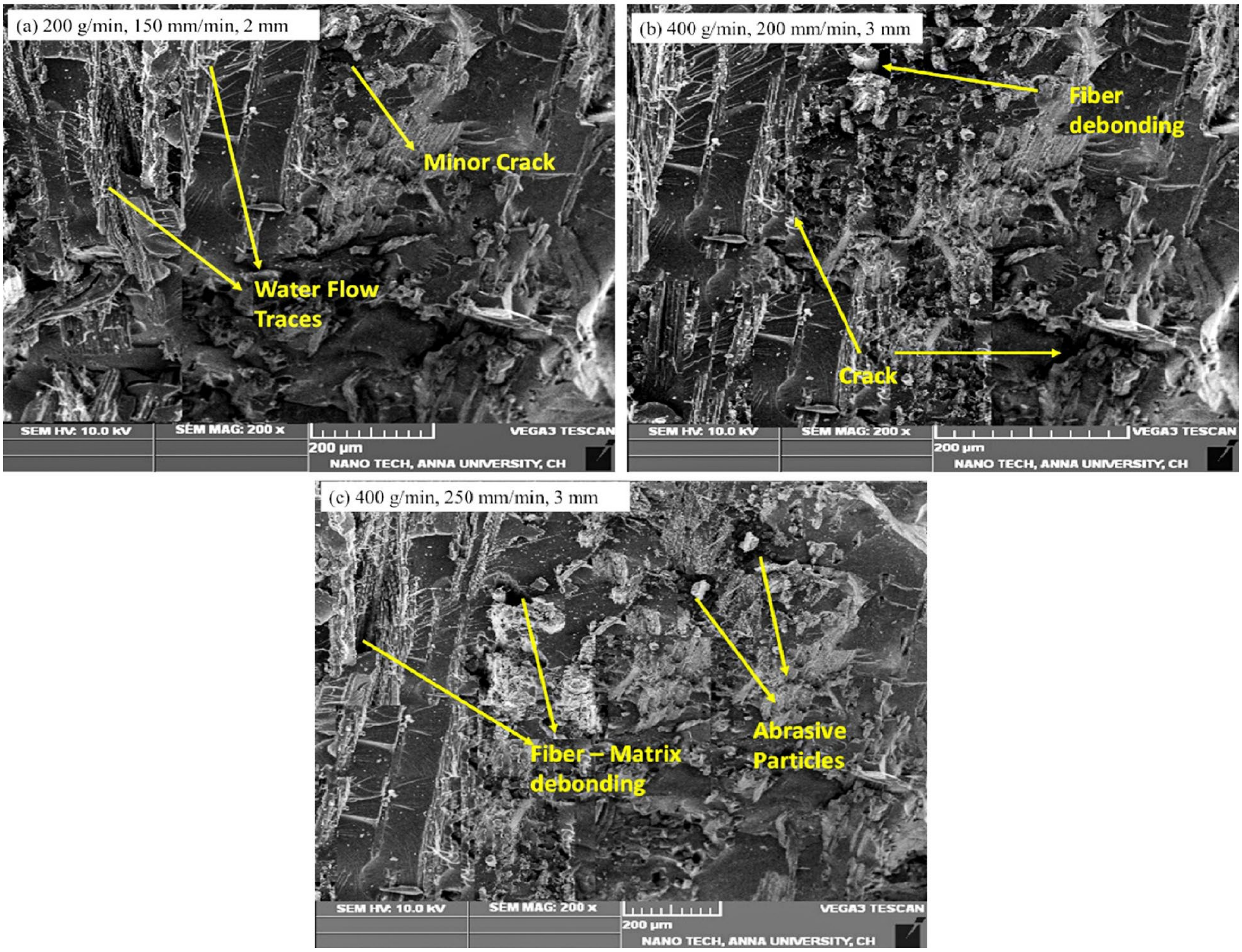

Fig. 16. (**a**-**c**) SEM analysis of AWJM sample.

SEM analysis of AWJM sample

SEM images of the AWJM-machined samples (Fig. 16) illustrate the morphology of the hybrid epoxy composites under different working conditions. In Fig. 16a, with an abrasive flow rate of 200 g/min, a traverse speed of 150 mm/min, and a SoD of 2 mm, the study observes minor cracks and water-flow traces on the surface. These conditions indicate that the relatively lower abrasive flow rate and speed result in minimal surface damage.

The small crack may be attributed to insufficient interaction between abrasive particles at low flow rates, leading to less aggressive material removal. The traces of water flow show that the force of the jet is sufficient to provide marks, however, not so high as to result in excessive fiber breakage or fiber-matrix debonding. The reduced traverse speed will help achieve a more controlled machining operation, minimizing the risk of fiber pullout and the formation of massive cracks. Figure 16b indicates more pronounced cracks and fiber debonding of AFR 400 g/min, TS 200 mm/min, and SoD 3 mm. An increased abrasive flow rate will bring more abrasive particles to the surface, thereby enhancing cutting force and positioning fibers within the matrix. The higher SoD makes the cracks more prominent by allowing the water jet to move aside, thereby damaging the fiber-matrix contact over a larger area. Not only does this faster jet movement across the surface result in less dwell time and more aggressive cutting (both of which lead to further fiber breakage and crack propagation), but it is also influenced by the higher traverse speed. Figure 16c shows that the largest parameters (400 g/min, 250 mm/min, 3 mm SoD) exhibit extensive fiber-matrix debonding and abrasive particles adhering to the surface. A destroyed fiber structure results from ripping the fiber structure at a high flow rate of 400 g/min, which uniformly disperses abrasive particles. This is further enhanced by the high rate of 250 mm/min, which disrupts the fibers due to the jet's high speed. In the meantime, even the large SoD undermines the material's structural integrity, distributing the jet's force over a wider span.

Conclusions

This study showed that a banana–paddy straw fiber reinforced epoxy composite can provide a useful balance between material performance and machinability, supporting the broader goal of developing sustainable composites from agricultural residues. Among the formulations studied, BP2 provided the most favorable overall combination of tensile, flexural, impact, thermal, moisture-resistance, and AWJM responses. The results further suggest that this behavior is related to improved fiber-matrix adhesion, lower void content, and more efficient load transfer, indicating that the banana-to-paddy-straw ratio plays an important role in determining both composite integrity and machining behavior. From a machining perspective, the work shows that AWJM is a suitable low-thermal-damage process for this hybrid composite system, and that the selected parameter window can reduce surface roughness and kerf angle while preserving cut quality. The broader contribution of the study is therefore not only the characterization of the developed hybrid composite, but also the demonstration that material design and machining optimization must be considered together for natural-fiber composite applications.

At the same time, this study has several limitations. Only three formulations were investigated, AWJM optimization was conducted only on the best-performing composition (BP2), and some interpretations remain qualitative, particularly those related to crystallinity and microstructure-property correlations. In addition, the conclusions are based on laboratory-scale testing within a limited range of AWJM parameters. Future work should therefore focus on broader compositional screening, statistical validation using replicate-based significance analysis, quantitative assessment of crystallinity, and long-term durability studies under environmental aging. It would also be valuable to extend the AWJM analysis to other compositions and expand the ANN dataset to improve predictive robustness across wider processing windows and for industrial-scale applications. The present results show that AWJM is a suitable machining approach for the developed banana–paddy straw hybrid composite, enabling favorable surface quality and kerf control under optimized conditions. While previous literature has discussed machining challenges in drilling, milling, and laser-based processing of composites, the present study did not perform a direct experimental comparison with those methods. Accordingly, the findings should be interpreted as demonstrating the effectiveness of AWJM for this material system rather than its universal superiority over other machining routes.

Data availability

Data will be made available on request.

Received: 25 February 2026; Accepted: 8 May 2026
Published online: 18 May 2026

References

1. Ramesh, G., Subramanian, K., Sathiyamurthy, S. & Prakash, M. *Calotropis Gigantea* fiber-epoxy composites: Influence of fiber orientation on mechanical properties and thermal behavior. *J. Nat. Fibers* **00**, 1–13 (2020).
2. Ahmad, F., Choi, H. S. & Park, M. K. A review : Natural fiber composites selection in view of mechanical, light weight, and economic properties. *Macromol. Mater. Eng.* https://doi.org/10.1002/mame.201400089 (2015).
3. Arora, G. et al. Recent Studies on Multiscale Modeling of Natural Fiber-Reinforced Composites. *Arch. Comput. Methods Eng.* https://doi.org/10.1007/s11831-025-10454-x (2025).
4. Yorseng, K. et al. Lightweight Innegra–hemp/epoxy hybrid composites: Effects of weathering on mechanical, thermal, and viscoelastic properties. *Int. J. Precis. Eng. Manuf.* https://doi.org/10.1007/s12541-025-01377-5 (2025).
5. Techawinyutham, L. et al. Sustainable epoxy composites from hemp/pineapple/glass fibers for lightweight automobile panels. *Int. J. Biol. Macromol.* **337**, 149392 (2026).
6. Todkar, S. S. & Patil, S. A. Review on mechanical properties evaluation of pineapple leaf fibre (PALF) reinforced polymer composites. *Compos. Part B Eng.* **174**, 106927 (2019).
7. Rajesh, M. & Pitchaimani, J. Mechanical characterization of natural fiber intra-ply fabric polymer composites: Influence of chemical modifications. *J. Reinf. Plast. Compos.* **36**, 1651–1664 (2017).
8. Haris, N. I. N. et al. Dynamic mechanical properties of natural fiber reinforced hybrid polymer composites: A review. *J. Mater. Res. Technol.* **19**, 167–182 (2022).
9. Yan, L., Chouw, N. & Jayaraman, K. Flax fibre and its composites - A review. *Compos. Part B Eng.* **56**, 296–317 (2014).
10. Kumar, V. V., Katamneni, P., Chandran, S. & Muflikhun, M. A. *Failure of Lightweight Composites: A Machine Learning Approach. Lightweight Composites: Mechanics, Processing, Properties, and Applications* (INC, 2025). https://doi.org/10.1016/B978-0-443-18852-7.00004-X.
11. Saha, A., Kumar, S., Zindani, D. & Bhowmik, S. Micro-mechanical analysis of the pineapple-reinforced polymeric composite by the inclusion of pineapple leaf particulates. *Proc. Inst. Mech. Eng. L J. Mater. Des. Appl.* **235**, 1112–1127 (2021).
12. Abd El-Baky, M. A., Attia, M. A., Abdelhaleem, M. M. & Hassan, M. A. Flax/basalt/E-glass Fibers Reinforced Epoxy Composites with Enhanced Mechanical Properties. *J. Nat. Fibers*. **19**, 954–968 (2022).
13. Ul Haq, M. Z. et al. Mechanical and durability performance of sisal, jute, and hemp fiber-reinforced concrete: Effects of chemical treatment and fiber geometry. *J. Nat. Fibers.* https://doi.org/10.1080/15440478.2025.2583855 (2025).
14. Costa, R. D. F. S., Sales-Contini, R. C. M., Silva, F. J. G., Sebbe, N. & Jesus, A. M. P. A critical review on fiber metal laminates (FML): From manufacturing to sustainable processing. *Metals* https://doi.org/10.3390/met13040638 (2023).
15. Varma, M., Chandran, S., Kumar, V., Suyambulingam, V., Siengchin, S. & I. & A comprehensive review on the machining and joining characteristics of natural fiber-reinforced polymeric composites. *Polym. Compos.* **45**, 4850–4875 (2024).
16. Kavimani, V., Gopal, P. M., Sumesh, K. R. & Kumar, N. V. Multi response optimization on machinability of SiC waste fillers reinforced polymer matrix composite using Taguchi's coupled grey relational analysis. *Silicon* **14**, 65–73 (2022).
17. Jagadish, Patel, G. C. M., Sibalija, T. V., Mumtaz, J. & Li, Z. Abrasive water jet machining for a high-quality green composite: the soft computing strategy for modeling and optimization. *J. Brazilian Soc. Mech. Sci. Eng.* **44**, 83 (2022).
18. Jani, S. P., Senthil Kumar, A. & Khan, M. A. Sujin Jose, A. Design and optimization of unit production cost for AWJ process on machining hybrid natural fibre composite material. *Int. J. Light Mater. Manuf.* **4**, 491–497 (2021).
19. Kesarwani, S., Verma, R. K., Ramkumar, J. & Jayswal, S. C. Production and machinability evaluation of reduced graphene oxide nanoparticles-reinforced polymer composites during abrasive water jet machining process. *J. Brazilian Soc. Mech. Sci. Eng.* **46**, 599 (2024).
20. Palanikumar, K., Prabhudass, J. M., Prabha, P. S. & Senthilkumar, N. Sustainable optimization of abrasive water jet machining for MWCNT/bamboo/Kenaf hybrid polymer composites. *Int. J. Interact. Des. Manuf.* **19**, 3765–3782 (2025).
21. Suyambulingam, I. et al. Banana peel waste as a source of cellulosic filler: Isolation, characterization, and its potential as a green reinforcement in polymer composites. *J. Mater. Cycles Waste Manag.* https://doi.org/10.1007/s10163-025-02374-6 (2025).
22. Thanikodi, S., Giri, J., Saravanan, R. & Mohammad, F. Eco-friendly alternatives to printed circuit boards: Developing natural fiber polymer composites with optimized flammability and moisture resistance. *J. Mater. Sci. Mater. Electron.* **36**, 1–16 (2025).
23. Vinoth, V., Sathiyamurthy, S., Jayabal, S., Saravanakumar, S. & Prabhakaran, J. Assessment of mechanical and morphological characteristics in polymer matrix composites reinforced with paddy pulp and pineapple leaf fibres. *Int. J. Mater. Eng. Innov.* **15**, 365–377 (2024).

24. Sathiyamurthy, S., Saravanakumar, S. & Vinoth, V. Enhancing tribological performance of hybrid fiber-reinforced composites through machine learning and response surface methodology. *J. Reinf. Plast. Compos.* **44**, 2306–2324 (2024).
25. Vishnu, V. & Kumar, K. S. Artificial Intelligence and Machine Learning for Sustainable Manufacturing: Current Trends and Future Prospects. *Intell. Sustain. Manuf.* **2**, 10002 (2025).
26. Singh, A. K. et al. State-of-the-art study on pineapple, coir, and banana fiber-reinforced composites: Mechanical, thermal, and durability performance. *J. Reinf Plast. Compos.* **0**, 1–43 (2025).
27. Brn, M., Beedu, R., Jayashree, P. K. & Potti, S. R. Study on machining quality in abrasive water jet machining of jute-polymer composite and optimization of process parameters through Grey Relational Analysis. *J. Compos. Sci.* https://doi.org/10.3390/jcs8010020 (2024).
28. Prabu, V. A., Kumaran, S. T. & Uthayakumar, M. Performance Evaluation of Abrasive Water Jet Machining on Banana Fiber Reinforced Polyester Composite. *J. Nat. Fibers*. **14**, 450–457 (2017).
29. Kalirasu, S., Rajini, N., Bharath Sagar, N. & Mahesh Kumar, D. Gomathi Sankar, A. Studies of Abrasive Water Jet Machining (AWJM) Parameters on Banana/Polyester Composites Using Robust Design Concept. *Appl. Mech. Mater.* **787**, 573–577 (2015).
30. Madival, A. S., Doreswamy, D., Shetty, R., Naik, N. & Gurupur, P. R. Optimization and prediction of process parameters during abrasive water jet machining of hybrid rice straw and *Furcraea foetida* fiber reinforced polymer composite. *J. Compos. Sci.* https://doi.org/10.3390/jcs7050189 (2023).
31. Dhilip, J. D. J. et al. Influence of Polybenzimidazole Nanofiller in Pineapple Fiber-Based Epoxy Composites: Tribological and Optimization Analyses. *Cellul Chem. Technol.* **59**, 1143–1155 (2025).
32. Ramachandran, A. R. et al. Multi-attribute optimization of drilling Carbon-Innegra fiber–reinforced composites using Entropy-TOPSIS. *Int. J. Adv. Manuf. Technol.* **139**, 3361–3379 (2025).
33. Saravanakumar, S., Sathiyamurthy, S. & Vinoth, V. Enhancing machining accuracy of banana fiber-reinforced composites with ensemble machine learning. *Measurement* **235**, 114912 (2024).
34. Periyappillai, G., Subbarayan, S. & Sengottaiyan, S. Advanced ensemble machine learning prediction to enhance the accuracy of abrasive waterjet machining for biocomposites. *Mater. Chem. Phys.* **333**, 130175 (2025).
35. Saravanakumar, S., Sathiyamurthy, S., Vinoth, V. & Devi, P. Effect of Alumina on epoxy composites with banana fiber: Mechanical, water resistance and degradation property analysis. *Fibers Polym.* **25**, 275–287 (2024).
36. Jayabal, S., Rajamuneeswaran, S., Ramprasath, R. & Balaji, N. S. Artificial neural network modeling of mechanical properties of calcium carbonate impregnated coir-polyester composites. *Trans. Indian Inst. Met.* **66**, 247–255 (2013).
37. Qureshi, M. N., Badgujar, A. & Khan, A. Investigation of chicken feather fiber / Poly-Lactic Acid reinforced composites prepared using the sandwich method. *Int. J. Mater. Eng. Innov.* **14**, 1 (2023).
38. Babu, M. N. & Muthukrishnan, N. Exploration on kerf-angle and surface roughness in abrasive waterjet machining using response surface method. *J. Inst. Eng. Ser. C* **99**, 645–656 (2018).
39. Sengottaiyan, S., Sathiyamurthy, S., Selvakumar, G. & Haridass, R. Influence of treatment and fly ash fillers on the mechanical and tribological properties of banana fiber epoxy composites: Experimental and ANN-RSM modeling. *Compos. Interfaces* **32**, 953–986 (2025).
40. Kannan, G. & Thangaraju, R. Evaluation of tensile, flexural and thermal characteristics on agro-waste based polymer composites reinforced with banana fiber/coconut shell filler. *J. Nat. Fibers.* https://doi.org/10.1080/15440478.2022.2154630 (2023).
41. Sumesh, K. R., Ajithram, A., Palanisamy, S. & Kavimani, V. Mechanical properties of ramie/flax hybrid natural fiber composites under different conditions. *Biomass Convers. Biorefinery*. **14**, 29579–29590 (2024).
42. Atmakuri, A., Palevicius, A., Vilkauskas, A. & Janusas, G. Numerical and experimental analysis of mechanical properties of natural-fiber-reinforced hybrid polymer composites and the effect on matrix material. *Polymers (Basel)* https://doi.org/10.3390/polym14132612 (2022).
43. Vijayaraj, S., Vijayarajan, K., Balaji, N. S. & Balaji, A. Conversion of finger millet husk waste as biosilica functional filler for *Digitaria ischaemum* fibre-epoxy composite: Fatigue, creep, and flame retardant behaviour. *Biomass Convers. Biorefinery* **14**, 21541–21551 (2024).
44. Dua, S. et al. Potential of natural fiber based polymeric composites for cleaner automotive component production - A comprehensive review. *J. Mater. Res. Technol.* **25**, 1086–1104 (2023).
45. B a, P., P Shetty, B., B, S., Singh Yadav, S. P. & L, A. Physical and mechanical properties, morphological behaviour of pineapple leaf fibre reinforced polyester resin composites. *Adv. Mater. Process. Technol.* **8**, 1147–1159 (2022).
46. Al-Jarrah, R. & AL-Oqla, F. M. A novel integrated BPNN/SNN artificial neural network for predicting the mechanical performance of green fibers for better composite manufacturing. *Compos. Struct.* **289**, 115475 (2022).
47. Biruk-Urban, K., Zagórski, I., Kulisz, M. & Leleń, M. Analysis of vibration, deflection angle and surface roughness in water-jet cutting of AZ91D magnesium alloy and simulation of selected surface roughness parameters using ANN. *Materials (Basel)* https://doi.org/10.3390/ma16093384 (2023).
48. Zhang, Z. & Friedrich, K. Artificial neural networks applied to polymer composites: A review. *Compos. Sci. Technol.* **63**, 2029–2044 (2003).
49. Liu, B., Vu-Bac, N., Zhuang, X., Fu, X. & Rabczuk, T. Stochastic full-range multiscale modeling of thermal conductivity of polymeric carbon nanotubes composites: A machine learning approach. *Compos. Struct.* https://doi.org/10.1016/j.compstruct.2022.115393 (2022).
50. Ang, J. Y., Abdul Majid, M. S., Mohd Nor, A., Yaacob, S. & Ridzuan, M. J. M. First-ply failure prediction of glass/epoxy composite pipes using an artificial neural network model. *Compos. Struct.* **200**, 579–588 (2018).
51. Iliyasu, I., Bello, J. B., Oyedeji, A. N., Salami, K. A. & Oyedeji, E. O. Response surface methodology for the optimization of the effect of fibre parameters on the physical and mechanical properties of deleb palm fibre reinforced epoxy composites. *Sci. Afr.* **16**, 1–11 (2022).
52. Kalirasu, S., Rajini, N., Rajesh, S., Seingchin, S. & Ramaswamy, S. N. AWJ machinability performance of CS/UPR composites with the effect of chemical treatment. *Mater. Manuf. Process.* **33**, 452–461 (2018).
53. Kumar, K. N. & Babu, P. D. Improving the machining performance of polymer hybrid composite by abrasive water jet machining for precise machining. *Arab. J. Sci. Eng.* **undefined**, 15347–15366 (2024).

Author contributions

Saravanakumar Sengottaiyan – Supervision, Writing Original Draft; **Muhemin Sheriff** – Software, Coding **; Shai Sundaram –** Visualization **; Yuvaraj-** Review and editing; **Ramalakshmi** – Validation; **Rajkumar** – Conceptualization, Resources, Review and editing.

Funding

There are no funding sources for this research work.

Declarations

Competing interests
The authors declare no competing interests.

Human and animal rights
This study does not involve human participants or animals. All experimental procedures were carried out exclusively on composite materials, ensuring compliance with ethical guidelines and research standards. No human or animal subjects were used or harmed during this study.

Additional information
Correspondence and requests for materials should be addressed to S.R.

Reprints and permissions information is available at www.nature.com/reprints.

Publisher's note Springer Nature remains neutral with regard to jurisdictional claims in published maps and institutional affiliations.